RecA-based patterning of DNA scaffolds

Student ID

Date

Major Code:

Supervisor Name:

A dissertation submitted in partial fulfillment
of the requirements for the degree of

( )

University Information

University Logo

Faculty Name

Contents

I. Acknowledgments

First I would like to thank my supervisors XXX who have given me lots of advice and encouragement throughout this project. A special thanks to my family who have given me the confidence to pursue a career in science and to XXX for supporting my decision to switch from music Bio. Finally, I would like to thank XXX for all her support over the last three years.

II. Abbreviations

SAM – Self-Assembled Monolayer

PL – Phospholipid

ACV – Alternating Current Voltammetry

CV – Cyclic Voltammetry

DME – Dropping Mercury Electrode

PC – Phosphotidyl Choline

PS – Phosphotidyl Serine

HMDE – Hanging Mercury Drop Electrode

AC – Alternating Current

DC – Direct Current

DOPC – Dioleoyl Phophotidyl Choline

CMC – Critical Micelle Concentration

PZC – Potential of Zero Charge

EDL – Electrical Double-Layer

IHP – Inner Helmholtz Plane

OHP – Outer Helmholtz Plane

SCE – Standard Calomel Electrode

RCV – Rapid Cyclic Voltammetry

NHE – Normal Hydrogen Electrode

SHE – Standard Hydrogen Electrode

PAH – Polyaromatic Hydrocarbon

DVT – Deep Vein Thrombosis

HGDE – Hanging Galinstan Drop Electrode

ASV – Anodic Stripping Voltammetry

PECVD – Plasma Enhanced Chemical Vapour Deposition

PTFE – Polytetrafluoroethylene

MW- Molecular Weight

EIS – Electrical Impedance Spectroscopy

ROS – Reactive Oxygen Species

III. Mathematical Terms and Constants

k – Boltzmann constant (1.33×10^{-23} J K^{-1})

R – Molar gas constant (8.3145J K^{-1} mol^{-1})

T – Absolute temperature (K)

σ – Stored charge density (µF cm^{-2})

ε – Dielectric constant

ε_o – Permittivity of free space (8.85419×10^{-14} F cm^{-3})

d – Parallel plate separation distance (cm)

C_{dl} – Double-layer capacitance (µF)

C_{sp} – Specific capacitance (µF)

C_H – Stern layer capacitance (µF)

C_D – Diffuse layer capacitance

Φ – Potential (V)

ΔG_m – Gibbs free energy of mixing (J mol^{-1})

ΔH_m – Enthalpy of mixing (J)

ΔS_m – Entropy of mixing (J K^{-1})

z – Charge (C)

F – Faraday's constant (9.6485×10^4 C mol^{-1})

$E^{\ominus}$ – Standard reduction potential (V)

E – Potential (V)

D – Diffusion co-efficient (cm^2 s^{-1})

A – Electrode area (cm^2)

f – Frequency (Hz)

Note: Units are given as they most commonly appear in this report

IV. Abstract

Phospholipid (PL) monolayers of Dioleoyl Phophotidyl Choline (DOPC) were supported by galinstan, gallium-indium (Ga-21.5%wt In) and 11.2%wt galinstan: mercury (Hg). AC voltammetry (ACV) scans show that three phase transitions occur on both Ga-In and galinstan alloys. For Ga-In these occur at ~ -1.21V, -1.28V and -1.48V vs Ag/AgCl/KCl reference. For galinstan they occur at ~ -1.13V, -1.18V and -1.44V vs Ag/AgCl/KCl reference. This is a 300mV and 200mV cathodic shift compared with Hg respectively. With rapid cyclic voltammetry (RCV), a large interfering current peak begins at just above -0.8V. This was attributed to hydrogen reduction however increasing the electrolyte pH increased the size of this peak. It was suggested that sodium hydroxide (NaOH) alkali buffer was not suitable. The Ga-In/0.1 mol dm^{-3} electrolyte interface yielded five characteristic peaks within the -1.1V to -1.8V window. Two reversible RCV phase transition peaks were also obtained using the 11.2%wt galinstan:Hg mix. Stable, reversible and reproducible phase transitions on Ga-In were obtained using RCV between -1.1V to -1.4V, these resemble those of Hg but shifted toward more negative potentials and with smaller resulting current.

V. Introduction

The aim of this project was to find out whether gallium (Ga) alloys could be used as a replacement for Hg in electrochemical sensing. Ideally the Ga alloys would be able to support a self-assembled PL monolayer on their surface that could then undergo re-orientations as the polarisation of the electric field changed. The phase transitions on Hg are detected as sharp capacitance peaks at well-defined potentials. It was of great interest to see whether the same phase transition peaks occurred on Ga alloys and at what potential. This project is a continuation of previous work at the University of Leeds that has developed a novel flow-system based around a microelectrode array. Liquid metals are deposited on to this array, which is housed within a flow-cell. This allows real-time monitoring of solutions passing over the working electrode surface and has attracted a great deal of interest from industry. It is hoped that the device can be implemented in *on-line* toxicity monitoring of water systems. The major drawback of the current system is that the toxic metal Hg is used. Non-toxic Ga alloys are much safer to use and would be environmentally favourable.

The first part of this report describes the self-assembly of covalently attached monolayers onto the surfaces of electrochemical sensors. Following on from this, the next section looks at the self-assembly of PL monolayers that are driven by non-covalent interactions. The pre-programmed chemical structures of PLs determine their self-assembly properties. The water insoluble surfactant used in this project was DOPC: its chemical structure tends to form lamellar aggregates that make it ideal for coating flat surfaces.

Chapter-2 looks at the thermodynamic theory behind the phase transition peaks. An introduction to Flory-Huggins theory is given as this formed the basis of the first mean-field theory of phase transitions developed by Leermakers and Nelson. Essentially, this takes a complex three-dimensional system and simplifies it into a two-dimensional lattice. The lattice sites/layers represent different components of the system. Interactions between the electrode surface and molecules in solution are given interaction parameters that weigh the probability of a particular interaction event occurring. The work of Leermakers and Nelson, has been superseded by modern Monte Carlo simulations, the results of which provide a solid theory of what is happening to the monolayer as the applied interfacial potential is altered.

The next part of the report tracks the development of electrical double layer (EDL) theory. EDL theory relates to electrode-electrolyte interactions, providing an explanation for the capacitance peaks. This is developed further in Chapter-3 whereby the electrochemical techniques used to isolate changes in the double-layer are examined – these include alternating current (AC) and cyclic voltammetry (CV) methods. The electrode used in this project is a modern microfabricated adaption of a standard three-electrode setup, first developed in the 1960s.

Chapter-4 looks at the potential bio-sensing applications of the device. The PL monolayer provides a cell membrane model that is highly applicable to toxicity sensing. Various proteins can be incorporated into the monolayer, making the model even more biologically relevant. The ability to study voltage gated ion-channels/carriers using a simple electrochemical method is a remarkable accomplishment and is an area of research that has not yet been fully explored.

The results from this project open up a new avenue of research proving that Ga alloys can be used as a viable alternative to Hg in electroanalytical studies. It has also been successfully shown that under the correct electrodeposition conditions eutectic Ga-In alloys support a stable monolayer. The reversible phase transitions peaks on Hg are also seen with Ga-In and as would be expected, the potentials at which they occur are different. Further development of the system is needed in order to achieve the same signal strength, stability and reproducibility of Hg.

1. Self-Assembly

1.1 Self-Assembled Monolayers for Electrochemical Sensing

The discovery that self-assembled monolayers (SAMs) could be adsorbed onto conductive surfaces and then be used as the sensing element for electrochemical analysis has been around for a number of decades [1]. Two-dimensional SAM structures allow the tailoring of electron transfer processes, which are the foundation of electrodic electrochemistry. An electrochemical sensor undergoes three sequential processes, recognition of an analyte, signal transduction and signal recognition (Fig 1) [1]. Signal transduction may involve changes in potential (potentiometry), current (amperometry) or impedance (impedance spectroscopy) whereby changes at the electrode-electrolyte interface are converted into an electrical signal.

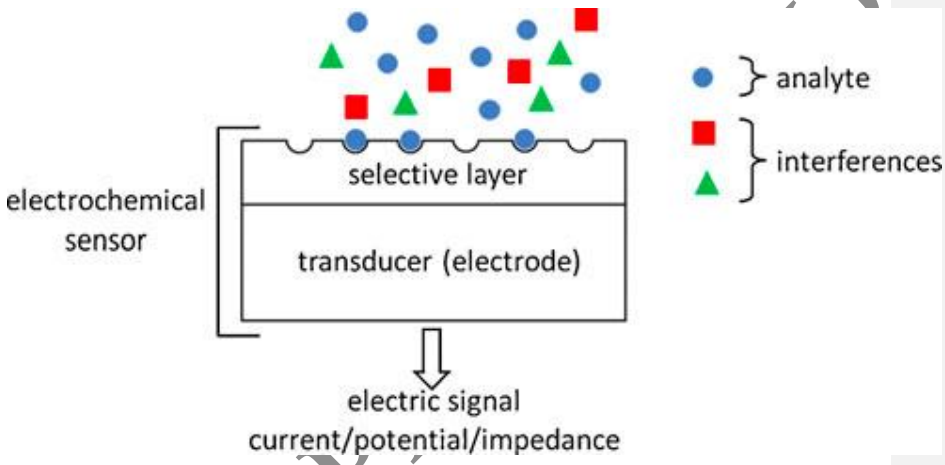

Figure 1. *Components of an electrochemical sensor [1]*

Events at the electrode-solution interface involve electron transfer, charge accumulation (capacitance) and adsorption/desorption events. Nearly all interactions are sensitive to the surface nature/morphology, hence why thin-film coatings as well as electrode material properties have such a profound effect on the sensing mechanism. The goal of sensor surface design is to maximise analyte-interface interactions, whilst suppressing interference from interfacial interactions [1].

The first SAMs on solid surfaces were alkylsilanes, which were covalently attached via a silane linkage [2]. During the 1980-90's, organosulfur SAMs were introduced and have subsequently attracted considerable attention due to their technological

implications [3-5]. Organosulfur SAMs are attached via a thiol linkage. Gold (Au) substrates were the original choice but Hg was later additionally used as support [6,7]. This was because Hg is a liquid metal, presenting an atomically smooth surface for deposition. Another reason is that thiols have a high affinity for Hg, hence why they are referred to as mercaptans from the latin *mercurium captans* (mercury capturing).

The structure and phase behaviour of thiol linked SAMs on Hg involves the subtle interplay of Van der Waals forces between neighbouring organic chains as well as the more complex interactions between end groups and the substrate [7]. The Hg-S bond strength is (~200kJmol^{-1}), which is comparable to the Au-S bond strength of (418kJmol^{-1}) [8]. With PLs there is no covalent bond linking the molecule to the surface, the self-assembly mechanism is primarily driven by the hydrophobic effect. When PLs are adsorbed onto an Hg electrode surface, changing polarity of the surface causes phase transitions i.e. re-orientation of the PL monolayer.

Miller et al [9] undertook the first electrochemical study of PL monolayers on Hg. The techniques they used were ACV and CV, using a dropping mercury electrode (DME). Monolayers of phopshatidylcholine (PC) and phosphatidylserine (PS) were studied in both their pure state and in the presence of polypeptides [9]. In the pure state a flat, low capacitance region (~1.6μFcm^{-2}) was observed until sharp phase transition capacitance peaks (adsorption/desorption) were seen at high positive and negative polarisations [9].

Nelson and Benton [10] furthered the development of PL monolayers at the Hg/ water interface. Instead of a DME, they used a hanging mercury drop electrode (HMDE), which was more stable and allowed studies on the same electrode surface to progress over extended periods, up to 3hrs [10]. They found that the HMDE system was very sensitive to “careless” procedure, which produced incomplete surface coverage, a disorganised film or a film that had impurities. This was recognised by irreproducibility and instability [10]. One of the major advantages of modern microfabricated electrode arrays is that they use much smaller electrodes that allow small volumes of electrolyte to be used, and as a result it is more difficult to introduce impurities into the system. The AC voltammogram (Fig 2) shows characteristic capacitance peaks for each of the four PLs (egg PC (a), dioleoyl PC (b), bacterial PE (c), bovine PE (d) [10].

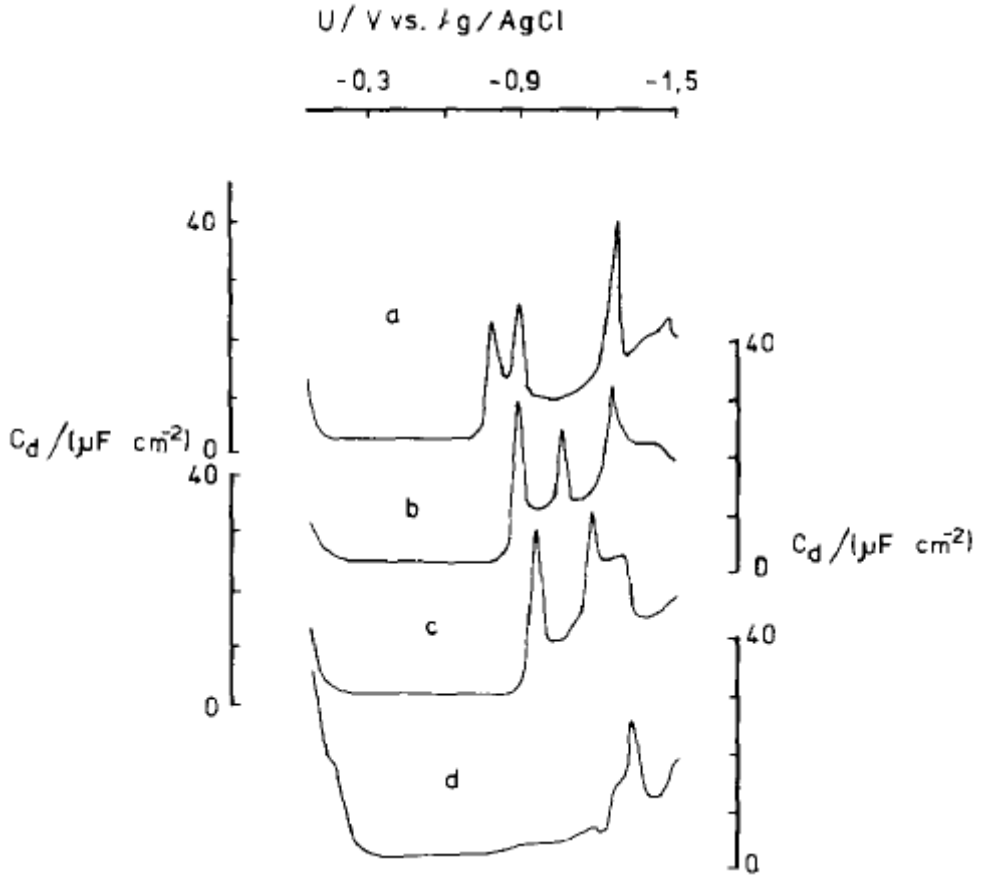

Figure 2. *AC voltammogram showing differential capacitance versus potential for four different PLs [10]*

The potential induced phase transitions in this project follow on from previous DOPC studies using Hg [11,12]. Nelson and Bizzotto [11] worked extensively with DOPC and used an AC waveform (75Hz, 4.5mV rms) superimposed onto a voltage ramp (scan-rate 5mVs^{-1}) to undertake capacitance measurements. Using the same Ag/AgCl reference electrode as this project, they found the DOPC monolayer showed two sharp capacitance peaks, one at -0.94V and the other at -1.02V [11]. These two peaks represent phase transitions of the monolayer. They also found that cathodic and anodic scans were exactly the same if the negative potential sweep did not go to potentials more negative than -1.1V [11]. A third peak appeared as the sweep was extended to -1.8V, after which the cathodic and anodic scans were markedly different. It was suggested that this was the point at which the monolayer was completely displaced from the surface and formed aggregate structures above the electrode surface

(micelles/bilayers). The phase transitions of DOPC have subsequently been modelled using Monte-Carlo simulations (Fig 3) [13].

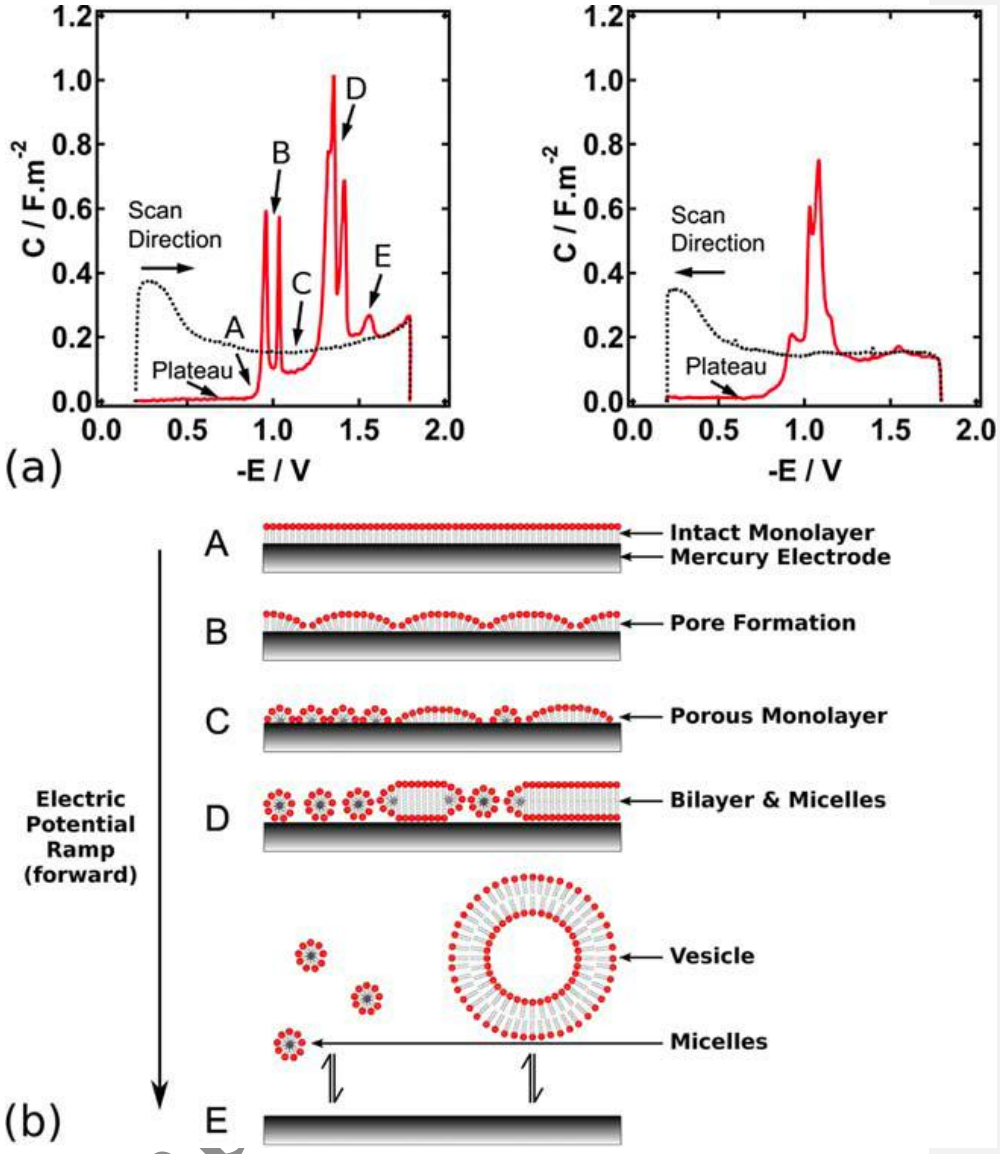

Figure 3. *Phase transitions for DOPC on Hg surface, showing formation of bilayer and micelles as the electrode potential becomes more negative. RCV forward and back scans presented separately, dotted line is bare electrode [13]*

1.2 Self-Assembly of Phospholipid Monolayers

DOPC is a zwitterionic water insoluble surfactant, which means it has both positive and negative charged regions that are displaced within the head group. It is also amphiphilic, meaning it has both apolar and polar regions. Figure-4 shows the structure of DOPC with the (N^+) group and (O^-) regions in the polar head group and the long apolar hydrocarbon tails. A surfactant is a portmanteau of surface-active-agent, this relates to the self-assembly properties of DOPC whereby in pure water it first forms a monolayer on the surface with the apolar region sticking out of the water and the polar head group facing into the water. At a critical micelle concentration (CMC) the surfactant forms spherical micelles. The point at which this occurs is different for each surfactant and can be measured via a potentiometric titration. If there are other solid surfaces in solution such as an electrode then the surfactant coats their surface, again with the head groups facing into the bulk solution and the hydrocarbon chains facing inwards [14,15].

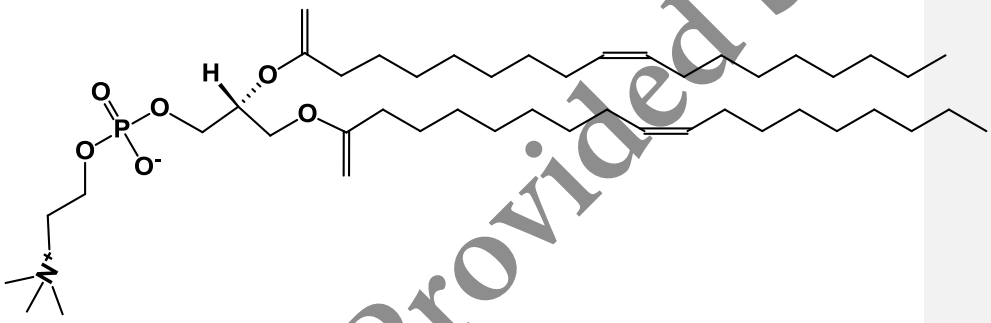

Figure 4. *Chemical structure of DOPC*

The inherent structure of water causes the "hydrophobic effect" that drives the self-assembly of PLs. Water has a fixed dipole, with a net negative charge on the oxygen atom and net positive charges on both hydrogen atoms. The opposing charges are separated by a 104.45^o bond angle. In order to satisfy these charges, hydrogen bonds form between hydrogen and oxygen atoms of neighbouring water molecules. Ions such as K^+ and Cl^- are attracted to the positive and negatively charged regions of water and thus become solvated. Similarly, the interactions of polar head groups and water molecules are enthalpically favourable, lowering the free-energy of the system. Apolar molecules cannot satisfy the charges of hydrogen and oxygen, and so water molecules

form hydrogen bonds around these regions, leading to highly ordered clathrate cages. This ordering of water produces a negative change in entropy, which is unfavourable, increasing the free-energy of the system. Therefore, the apolar regions of the surfactant spontaneously self-assemble so that they are not in contact with water, this releases water molecules from an ordered state into a more disordered state and so the self-assembly mechanism of PLs is primarily driven by a positive entropy change.

The Hg surface near the potential of zero charge (PZC) is apolar [16]. Highly competitive self-assembly processes lead to a compact monolayer that represents the outer-leaflet of a lipid bilayer. As the potential of the Hg changes, either positively or negatively away from the PZC, the surface becomes polar [16]. This results in two phase-transitions that are identified as two capacitance peaks, with a third capacitance peak reported to be desorption. Despite the simplicity of this statement, the statistical thermodynamic theory proving the phase transitions is complicated and not fully understood. The complexity arises from the fact that there are many different parameters, which introduce a large number of adaptations to the standard EDL/self-assembly models [13].

1.3 Flory-Huggins Theory

The following explanation of Flory-Huggins theory is adapted from [17-21].

Flory [20] and Huggins [21] developed a theory for understanding the non-ideal behaviour of polymers in solution, using a simple lattice model. The lattice sites in the Flory-Huggins model represent the size of the solvent molecules. If the molecular weight (MW) of the solvent is the same as the MW of the solute, then only one molecule of each can occupy a lattice site (Fig 5) making this an ideal and simplest model.

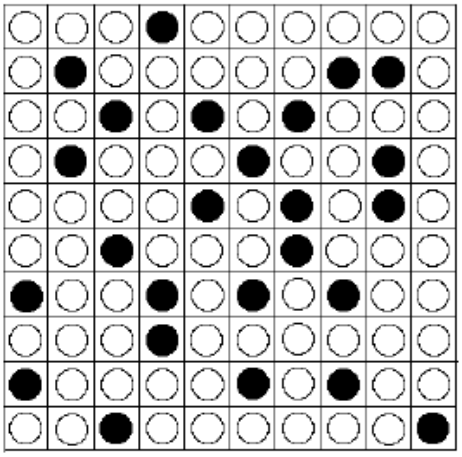

Figure 5. *Flory-Huggins lattice, black dots represent solute molecules, clear dots represent solvent molecules [17]*

The Boltzmann relation gives the increase in entropy due to mixing of the two components (ΔS_m).

$$\Delta S_m = k \ln \Omega \quad (1)$$

$\Delta S_m =$ change in entropy due to mixing

$k =$ Boltzmann's constant ($1.33\text{x}10^{-23}\text{JK}^{-1}$)

$\Omega =$ total number of ways of arranging n_1 (solvent molecules) and n_2 (solute molecules)

$$\text{N} = n_1 + n_2 = \text{total number of lattice sites} \quad (2)$$

The probability function $\Omega = \frac{\text{N!}}{n_1 + n_2}$

This leads to an expression for the entropy change of mixing each individual molecule: -

$$\Delta S_m = -k(n_1 \ln x_1 + n_2 \ln x_2) \quad (3)$$

Or for the molar entropy

$$\Delta S_m = -R(x_1 \ln x_1 + x_2 \ln x_2) \quad (4)$$

$R =$ molar gas constant ($8.3145\ \text{JK}^{-1}\text{mol}^{-1}$)

$x_1 =$ mole fraction of the solvent

$$x_1 = \frac{n_1}{n_1 + n_2} \tag{5}$$

The entropy of mixing (ΔS_m) for an ideal solution (solvent and solute have the same MW) is larger than the entropy of mixing for a low MW solvent and a high MW polymer e.g. DOPC. This is because of the loss of conformational entropy due to the linked tail region. To account for this in an expression of $\Delta S_{m,}$ the tail region is divided into sections (r), which are assumed to have the same MW as the solvent, (Fig 6). Therefore, (r = polymer volume: solvent volume) i.e. one lattice site. For n_2 polymer molecules, $N = n_1 + rn_2$

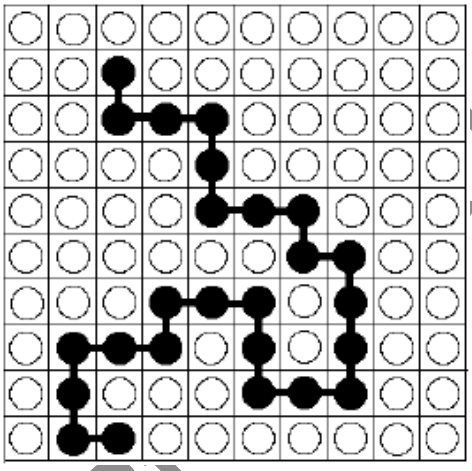

Figure 6. *Polymer chain segments in solvent lattice*

The Flory-Huggins expression for entropy becomes: -

$$\Delta S_m = -k(n_1 \ln \square_1 + n_2 \ln \square_2) \tag{6}$$

$\square_1 =$ lattice volume of solvent

$\square_2 =$ lattice volume of polymer

$$\square_1 = \frac{n_1}{n_1 + rn_2} \tag{7}$$

$$\square_2 = \frac{rn_2}{n_1 + rn_2} \tag{8}$$

The Flory-Huggins expression gives the entropy term for the Gibbs free energy calculation.

$$\Delta G_m = \Delta H_m - T\Delta S_m \quad (9)$$

The Flory-Huggins expression for enthalpy of mixing (ΔH_m) is: -

$$\Delta H_m = z n_1 r_1 \square_2 \Delta\omega_{1-2} \quad (10)$$

$z = \text{lattice co} - \text{ordination number}$

$r_1 = \text{number of segments in a solvent molecule}$

$\omega_{1-2} = \text{change in internal energy } (\Delta U_m) \text{ as a result of forming the solvent} -$ polymer pair (1-2)

ω_{1-2} is given by the mean field expression

$$\Delta\omega_{1-2} = \omega_{1-2} - \frac{1}{2}(\omega_{1-1} + \omega_{2-2}) \quad (11)$$

1-1 = solvent-solvent interactions

1-2 = solvent-polymer interactions

2-2 = polymer-polymer interactions

For DOPC: 1) tail-water interactions
2) head group-water interactions
3) tail-head group interactions
*4) Chain stiffness

z and ω_{1-2} can be combined into a single Flory interaction parameter X_{1-2}:-

$$X_{1-2} = \frac{z r_1 \Delta\omega_{1-2}}{kT} \quad (12)$$

Note: X_{1-2} is inversely proportional to temperature but independent of concentration

$T = \text{absolute temperature (K)}$

This gives the enthalpy of mixing (ΔH_m): -

$$\Delta H_m = kT X_{1-2} n_1 \square_2 \quad (13)$$

Finally, combining ΔS_m and ΔH_m gives the Flory-Huggins expression for the Gibbs free-energy of mixing a polymer in a solvent.

$$\Delta G_m = kT(n_1 \ln \square_1 + n_2 \ln \square_2 + X_{1-2} n_1 \square_2) \qquad (14)$$

Flory-Huggins theory presents the simplest lattice model for interactions involving long-chain molecules in solution. Leermakers and Nelson [16] used this as the starting point for a more complicated theory that takes into account the Hg-electrolyte interface, the polarity changes at the electrode surface and the polarity of the PL head groups. The following section is adapted from their publication [16] and follows on from the basic outline of Flory-Huggins theory.

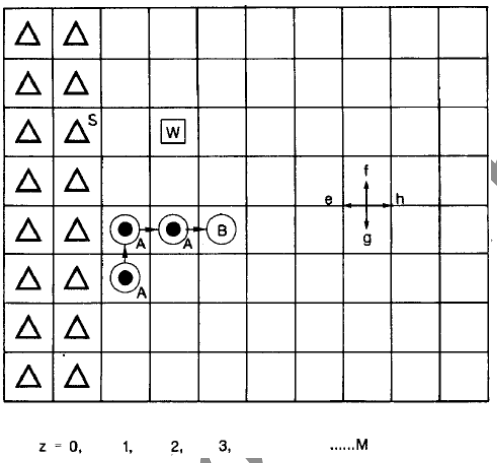

Figure 7. *Leermakers and Nelson's lattice, the triangles represent the solid electrode surface, W is the water (solvent), A are apolar segments of the polymer chain, B are polar segments, z = 0,1,2….M are the layers, e, f, g, h, are the second co-ordinates relating to segment number [16]*

Figure-7 shows a 2D lattice that represents the various interactions. The lattice layers are numbered Z = 0,1,….M with M being an arbitrary layer in the bulk solution. At M, inhomogeneities due to the boundary layer (z = 0) are absent i.e. at a certain distance from the solid (S) only solvent molecules are present. The volume fraction (see equation 7) for the solid electrode (z = 0) is $\square_s = 1$, for all other layers $\square < 1$. Although the layer z = 0 is completely filled, its role is crucial as it accounts for all the other interactions the solid has with the polymer segments and solvent (W).

The co-ordination number (z) (equation 10) gives the number of direct neighbours. A fraction of them will be in the previous layer (λ-1), a fraction in the layer of interest (λ_0) and a fraction in the next layer ($\lambda_1 = 1 - \lambda_0 - \lambda\text{-}1$). In the case of a co-polymer such

as DOPC, two types of segment (*r*) (equation 7) exist. These are non-polar chain groups (A) and polar head groups (B) (Fig 7). Therefore, a co-polymer denoted as $A_{12}B_2$ would have 12 non-polar segments and 2 polar segments. Again, the assumption is that the segments have the same volume as the solvent and are of similar MW.

The term (*x*) is used to denote an arbitrary segment type i.e. *x* = S, W, A or B. The layer dimension is expressed by (*L),* this is the number of lattice sites, which is equal for each layer. Each layer is then considered individually by considering the volume fraction (equation 15).

$$\square_x(z) = n_x(z)/L \tag{15}$$

$\square_x(z) =$ Volume fraction of x in layer z

$n_x(z) =$ number of sites in layer z occupied by segments of type x

Therefore, the weighted average volume fraction over the three layers (λ_{-1}, λ_0, λ_1) is: -

$$\langle \square_x(z) \rangle = \lambda - 1 \square_x(z-1) + \lambda_0 \square_z(z) + \lambda_1 \square_z(z+1) \tag{16}$$

The site fractions give the probability of finding a segment *x* next to a lattice site in layer *z*. The *z* contacts are weighted by a Flory-Huggins interaction parameter X_{x-y} (equation 12), which gives the free-energy difference (units of *kT*) for exchanging one segment (*x*) from an environment of pure *x* with a segment *y* from a pure *y* environment. Therefore, positive X_{x-y} values represent repulsion between segments, whilst negative X_{x-y} corresponds to attraction. The contact energy of a segment *x* in a lattice layer *z* is: -

$$\frac{u_x(z)}{kT} = \sum_y X_{x-y} \langle \square_y(z) \rangle \tag{17}$$

Note, the use of volume fractions relates to a mean-field approximation i.e. only averaged energy contacts are counted.

Flory-Huggins theory provides a simple way of qualitatively assessing the interactions between the various segments. The next stage in the mean-field theory becomes much more complicated as *chain stiffness (equation 11) is taken into account. This refers to

the ratio of *trans* to *gauche* bonds that are in the tail region. *Gauche* bonds add to chain stiffness and have a profound effect on the number of conformations that a polymer can have. DOPC has one double bond in each of its two hydrocarbon chains (Fig 4). This allows a good degree of chain flexibility, making it suitable for compact monolayer packing. Another reason why DOPC is a good choice for coating flat surfaces is its tendency to form flat lamellar aggregates in solution, rather than vesicles. DOPC exhibits a small, negative spontaneous curvature (-1/20 $J_s(nm^{-1})$), this is due to the volume of the head group being slightly smaller than the volume of the hydrocarbon tails (Fig 8) [22-24].

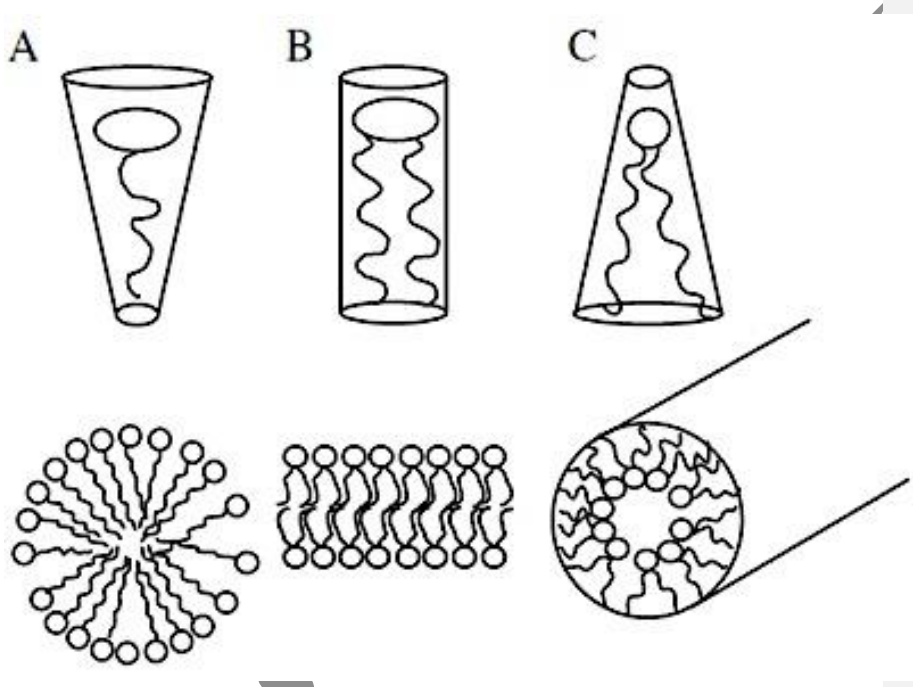

Figure 8. *Three types of PL with different ratios of head-group to total volumes, and associated packing arrangements (DOPC (B) [25]*

As well as chain stiffness, electrode-electrolyte interactions and self-assembly forces must also be factored into the Flory-Huggins theory. This makes the model even more complicated, requiring computer simulations [13]. The sharp capacitance peaks are clearly related to changes at the electrode-electrolyte interface, more specifically, changes to the structure of the EDL. Dr A. Vakourov at the University of Leeds has been using Atomic Force Spectroscopy (AFS) and confocal microscopy techniques to prove *in-situ*, the phase transitions predicted by the computer simulations.

2. Electrical Double-Layer Theory

2.1 Helmholtz Model

Hg is a good conductor therefore it does not support an electric field within itself at equilibrium. Helmholtz was the first to realise that a layer of specifically adsorbed ions was the reason charge was stored at the electrode surface. This meant that there were two sheets of opposite charge, the ions at the surface and the counter-ions in the solution. This structure is analogous to a parallel plate capacitor, where charge is stored on two metallic plates separated by a dielectric (polarisable) material, usually a ceramic (until $q=CE$ is satisfied). The relationship between stored charge density and potential drop across the plates is [26,27]: -

$$\sigma = \frac{\varepsilon\varepsilon_0}{d}V \tag{18}$$

$\sigma =$ stored charge density (μF cm^{-2})
$\varepsilon =$ dielectric constant
$\varepsilon_0 =$ permittivity of free space (8.85419 x 10^{-14} F cm^{-3})
$d =$ plate separation (cm)
$V =$ potential drop between plates (V)

Following on from this, the differential capacitance is therefore: -

$$\frac{\partial\sigma}{\partial V} = C_d = \frac{\varepsilon\varepsilon_0}{d} \tag{19}$$

The Helmholtz model predicts that capacitance is a constant (equation 19). However measuring differential capacitance as a function of potential shows that in low concentration electrolyte solutions, there is a dip in capacitance at the PZC i.e. the point at which the sign of the electrode switches and no net charge exists (Fig 9). This suggests that a more detailed model is required that takes into account the capacitance of the counter ions that are not specifically adsorbed onto the surface.

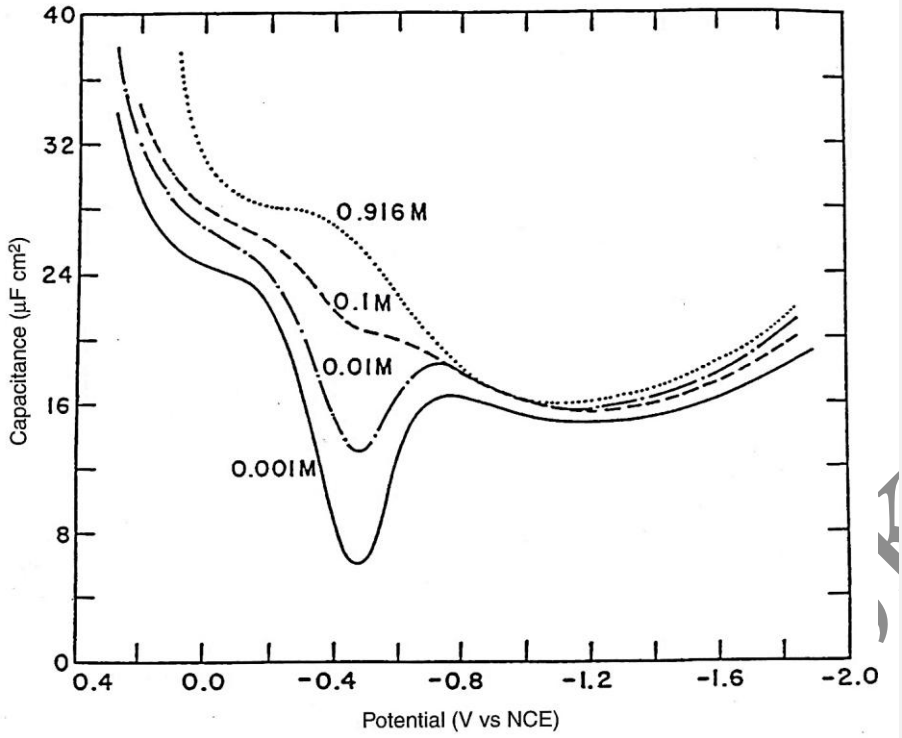

Figure 9. *Differential capacitance vs potential using a DME, with varying concentrations of NaF [28]*

Figure-9 shows that variations in potential and electrolyte concentration have a profound effect on capacitance, which means either ε or d depends on these two variables [29,30].

2.2 Goüy-Chapman Model

At low concentrations of electrolyte i.e. solutions with a low charge density, it takes a considerable thickness to accumulate enough excess charge to counterbalance the opposite charge at the electrode surface. Goüy and Chapman introduced the concept of a diffuse layer. Their model supposes that the greatest concentration of counter ions would be adjacent to the surface, where attractive electrostatic forces ($zF\Phi$) are able to overcome dispersive thermal motion (RT) (equation 20). Moving away from the surface, there is an exponential decay in the concentration of counter -ions until a point in the bulk solution where the concentrations of co-ions and counter-ions may be

considered equal. The Boltzmann equation relates the concentration of counter-ions at a given distance from the surface $C(x)$ and the electrostatic/ thermal forces: -

$$C(x) = C(0)e^{-(zF\square/RT)} \quad (20)$$

$C(0) =$ concentration of ionic species at the surface (mol dm^{-3})

$z =$ charge (F)

$\square =$ potential (V)

$R =$ molar gas constant (8.3145J K^{-1} mol^{-1})

$T =$ absolute temperature (K)

The Goüy-Chapman model altogether ignores the specifically adsorbed ion layer predicted by Helmholtz.

2.3 Stern Model

The failure of the Goüy-Chapman model is that it treats the ionic species as point charges, which allows them to approach the surface arbitrarily closely. Therefore, at high polarisations the exponential decay distance decreases until it reaches zero i.e. no separation between the metallic and solution-phase charge regions. Stern realised that in reality, ions could only approach the surface by finite amounts. Ions that had shed their hydration shells could become specifically adsorbed as proposed by Helmholtz. In the Stern model, an imaginary inner Helmholtz plane (IHP) runs through the centre of the adsorbed ions, whilst another imaginary outer Helmholtz plane (OHP) passes through the centre of ions that have approached as close to the surface as they can with their hydration shells attached. Together, the two planes make up the Stern layer, with the diffuse layer extending from the OHP into the bulk solution.

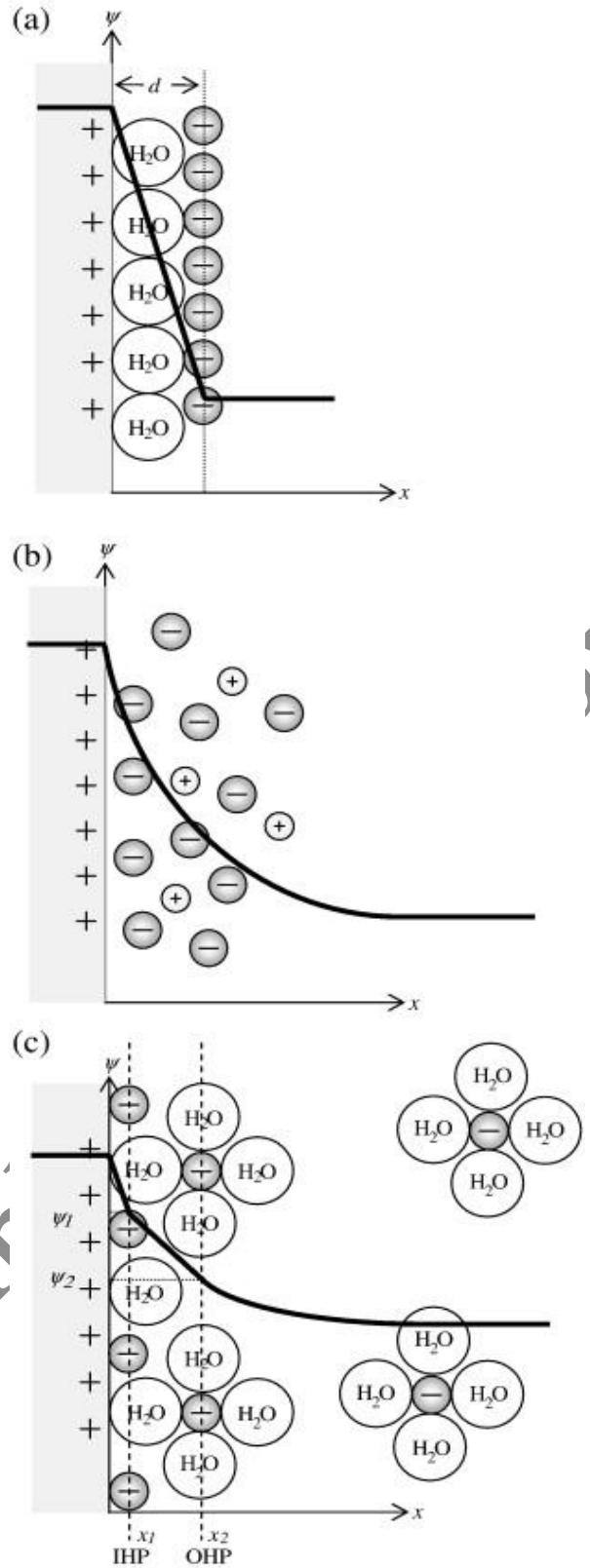

Figure 10. *a) Helmholtz model, b) Goüy-Chapman model, c) Stern model [31]*

From the Stern model, the capacitance of the double layer (C_{dl}) is a combination of the Stern layer (C_H) and diffuse layer (C_D) in series: -

$$\frac{1}{C_{dl}} = \frac{1}{C_H} + \frac{1}{C_D} \tag{21}$$

The smaller of the two capacitances dictates the observed behaviour of the double layer. Whilst the capacitance of the Stern layer is largely independent of concentration, the capacitance of the diffuse layer is strongly affected by changing electrolyte concentration (Fig 9). Figure-11 shows that at high electrolyte concentrations the observed capacitance of the double layer is purely a result of the charge stored at the electrode surface, whilst at low concentrations the capacitance of the diffuse layer begins to have a more pronounced effect. Therefore, in this project high concentrations of electrolyte were used so that any changes in capacitance can be more readily attributed to changes in the surface structure (phase transitions).

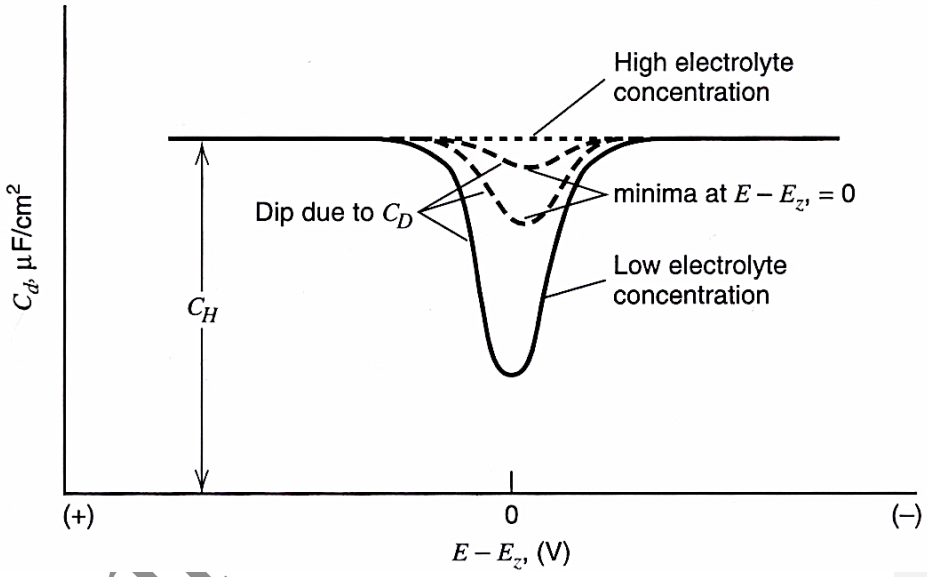

Figure 11. *Capacitance of Stern and diffuse layers at varying concentrations of electrolyte [26}*

Measuring the PZC of Hg on a HMDE is fundamental electrochemistry and should be relatively straightforward because of the atomically flat and homogenous surface for adsorption. Measuring the PZC for polycrystalline solids is more difficult due to surface roughness. For example, the PZC for silver (Ag) (111) is (-0.69V vs SCE) whilst Ag (110) is (-0.98V vs SCE) [26]. Because a solid electrode presents many

exposed crystal faces to a solution, different regions of the same surface can store different charge. For an electrode held at -0.8V versus the standard calomel electrode (SCE), the (111) sites will be negative of the PZC and thus carry negative charge whilst the (110) will carry positive charge [26]. These variations in stored charge density have a profound effect on capacitance measurements and therefore affect catalytic as well as adsorptive properties [27]. One of the problems of using a liquid metal electrode on top of a microelectrode array such as Pt on silicon nitride (Si_4N_3) is that exposed areas of the underlying metal can affect PZC/ double layer studies.

3. Studying Electrode Reactions

3.1 Cyclic Voltammetry

CV is the most commonly used technique for extracting qualitative information about electrochemical processes. CV is often the first experimental method used in electroanalytical studies because of its ability to provide important information about the thermodynamics of redox processes, electron transfer kinetics, coupled chemical reactions and adsorption/desorption processes [27].

During CV, a triangular potential waveform is linearly scanned at a stationary working electrode (Fig 12). Throughout the forward and reverse scans, a potentiostat records the current as a function of the applied potential. The resulting plot of current (*i*) versus potential (E) is referred to as a cyclic voltammogram (Fig 13). By convention, the potential is first scanned towards more negative values. For studying redox reactions it is assumed that all the species in solution are initially in their oxidised state, a starting potential is then chosen whereby no reduction takes place. As the potential approaches the characteristic standard reduction potential ($E^{\ominus}$) a cathodic current peak occurs. Reduction continues at a decreasing rate up until the switching potential (usually at least 90/n mV beyond the peak), at which point the working electrode becomes anodic. The species that has just been reduced is re-oxidised and an anodic peak is observed [27].

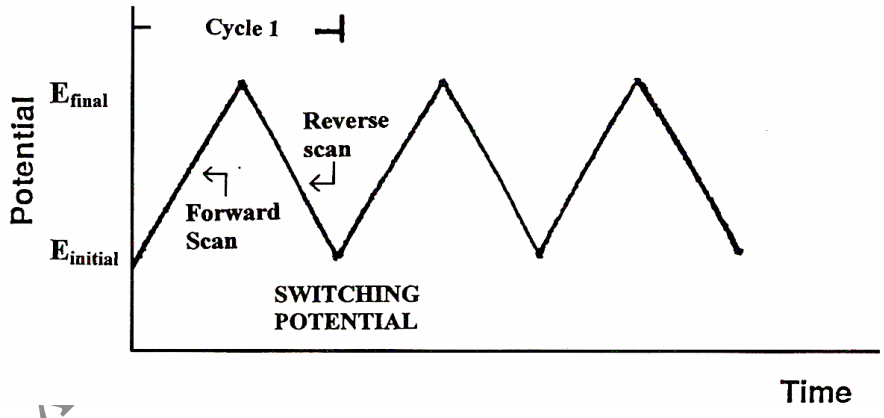

Figure 12. *Potential ramp [27]*

Slow ramps allow the ionic species in solution to transfer electrons at the surface and as a result, the faradaic current will be substantial whilst the capacitance current will

be small. At increased scan rates, the capacitance current becomes more significant in comparison to any faradaic current. At fast scan rates the charge transfer to electro-active species becomes negligible [32]. Comparing the forward and reverse scans provides useful information on the rates and reversibility of processes at the working electrode. Redox processes as governed by the Nernst equation (equation 22) are often complex and irreversible. Note, hydrogen reduction is inherently irreversible, forming a gas phase that rapidly leaves the working electrode surface.

$$E = E^{\ominus} - \frac{RT}{nF} \ln \frac{[Red]}{[Ox]} \quad (22)$$

$E =$ potential (V)

$E^{\ominus} =$ standard reduction potential (V)

$n =$ number of electrons transferred

$R =$ molar gas constant (8.314J K^{-1} mol^{-1})

$F =$ Faraday's constant (96,485 C mol^{-1})

$T =$ absolute temperature (K)

$\frac{[Red]}{[Ox]} =$ concentration of reduced to oxidised species (mol dm^{-3})

For this project, RCV has been chosen i.e. potential ramps greater that $1Vs^{-1}$. This means that capacitance current dominates cyclic voltammograms. For pure capacitance plots the forward and reverse scans are symmetrical and the integral of current is ($\int idt = 0$) (the cathodic/anodic peak areas are the same). For RCV at constant ramp rates, the current is directly proportional to capacitance.

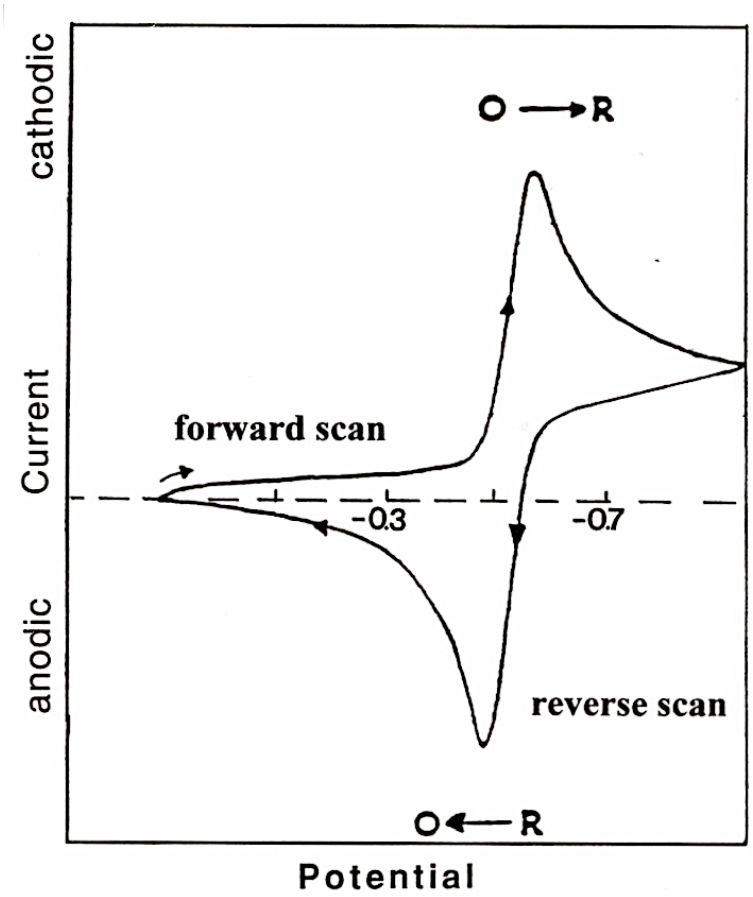

Figure 13. *Reversible cyclic voltammogran [27]*

At a constant scan rate, the current can therefore be calculated from: -

$$C_d = \frac{i}{\left(\frac{dV}{dt}\right)} \tag{23}$$

With the electrode surface acting as an ideal capacitor, the current is also directly proportional to the electrode area '*A*' (cm^2) (equation 24) and hence the term specific capacitance (C_{sp}) is introduced: -

$$C_{sp} = \frac{i}{\left(\frac{dV}{dt}\right)A} \tag{24}$$

Specific capacitance assumes a homogenous surface, as is the case with Hg. Current deviates from ideal behaviour for heterogeneous surfaces such as poorly combined alloys and microelectrodes, where the effects of the underlying conductive layer can be significant.

3.2 Factors Affecting Reaction Rates at the Electrode-Electrolyte Interface

There are two main factors affecting reaction rates (current) at the electrode-electrolyte interface. Mass transfer limited processes involve the migration of species from the bulk solution into the electrode surface region. This is a non-faradaic process meaning no electrons are transferred between species. Mass-transfer limited processes are reversible producing cyclic voltammograms resembling figure-13. From potential step techniques, the resulting diffusion controlled current (i) can be calculated using the Cottrell equation: -

$$i = \frac{nFAC^o\sqrt{D}}{\sqrt{\pi t}} \quad (25)$$

$n =$ number of electrons transferred
$F =$ Faraday′s constant (96,485 C mol^{-1})
$A =$ area of electrode (cm^2)
$C^o =$ intial concentration of reducible analyte (mol cm^{-3})
$D =$ diffusion coefficient ($cm^2 s^{-1}$)
$t =$ time (seconds)

Faradaic reactions involve the transfer of electrons from the electrode surface to an ion in solution. Electron transfer limited processes produce irreversible CV profiles. Other factors affecting reaction rates include chemical reactions and adsorption/desorption processes. These can produce quasi-reversible CV profiles (non-symmetrical but with ($\int idt = 0$). In reality, most electrode-electrolyte reactions involve a combination of different processes with the slowest one being the rate-determining step (Fig 14). Special techniques must be employed to isolate faradaic and non-faradaic contributions.

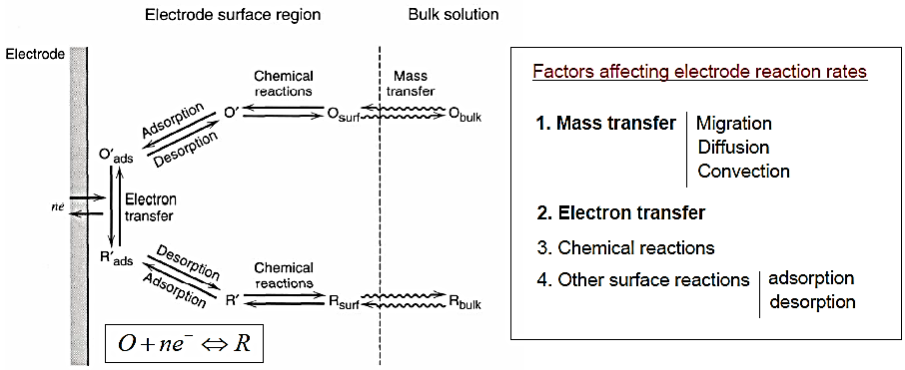

Figure 14. *Electrode-electrolyte processes, adapted from [26]*

3.3 Alternating Current Electrochemistry

Applying an alternating potential to an electrode produces an alternating current without the need for charge transfer across the electrode-electrolyte interface. In AC electrochemistry resistance becomes impedance (z), and because it is a sine wave it has not only amplitude but also frequency and phase. Measuring impedance requires a potentiostat equipped with a lock-in amplifier or electrical impedance spectroscopy (EIS) module. From impedance it is possible to calculate a circuit element's ability to resist current flux, which is frequency dependant. Measuring impedance over a range of frequencies and defined potentials permits a more detailed characterisation of electrode surfaces than using direct current (DC) techniques alone [26,27].

3.4 AC Voltammetry

For AC voltammetry, small amplitude, single frequency AC potential is superimposed onto a voltage ramp at the end of each potential step. The sine wave modulation allows impedance and capacitance signals to be isolated over a voltage range. For capacitance, the current is measured out of phase (-90°). The AC voltammetry technique is useful for understanding adsorption events (Fig 14) but is a much slower process than RCV, which can yield similar information. Specific capacitance (C_{sp}) is directly proportional to current: -

$$C_{sp} = \frac{i}{2\pi f \, \Delta \, VA} \tag{26}$$

f = frequency (Hz)

A = area (cm^{-2})

The other symbols have their usual meaning.

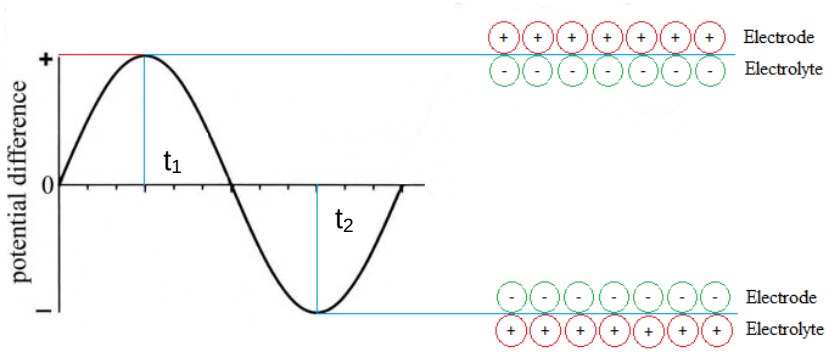

Figure 15. *AC voltammetry and the double layer*

Figure-15 shows how the electrode-electrolyte polarity is affected by the modulating potential. This rapid switching helps to remove the faradaic contributions during voltage ramps.

3.5 Three-Electrode Setup

Throughout this project, a standard three-electrode setup was used i.e. a reference electrode, working electrode and counter electrode. A reference electrode has known potential and as the name implies, acts as a reference point by which the working electrode potential is compared. This is analogous how altitude is measured by using sea level as a reference. The working electrode is where the reactions of interest occur, whilst the counter/auxiliary electrode is a current-carrying electrode, usually an inert metal such as Pt. The Ag/AgCl/KCL reference electrode (as used in this project) has a smaller temperature coefficient than the standard calomel electrode (SCE) and normal hydrogen electrode (NHE).

Early experiments used the NHE as the standard of zero potential. This electrode is difficult to use and involves a Pt electrode being immersed in strong acid with hydrogen being bubbled over the surface at around 1atm. The dangers of using strong acid as well as the difficulty in maintaining a constant hydrogen pressure and the aforementioned temperature sensitivity meant that the NHE was replaced by the standard hydrogen electrode (SHE). The SHE is a theoretical electrode-solution

interface where the concentration of hydrogen ions is 1mol dm^{-3} and they are assumed to have no interaction with other ions in solution. This has now become the standard for zero potential quoted in reduction potential tables [26,27].

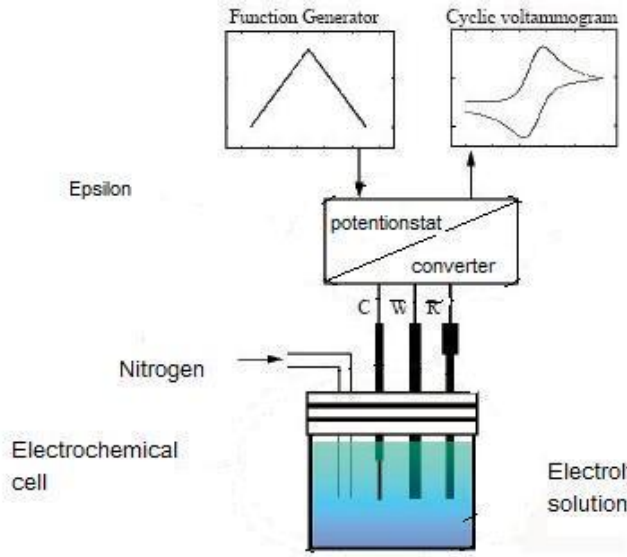

Figure 16. *Three-electrode setup as used in CV [33]*

Figure-16 shows a standard three-electrode cell as used in cyclic voltammetry. An inert gas purges the electrochemical cell of oxygen. This prevents interference caused by dissolved oxygen reduction. Oxygen reduction occurs via two well-separated two-electron steps: -

$$O_2 + 2H^+ + 2e^- \rightarrow H_2O_2 \qquad \text{Step 1}$$

$$H_2O_2 + 2H^+ + 2e^- \rightarrow 2H_2O \qquad \text{Step 2}$$

The reduction potentials of these two redox processes occur within the potential window used for most electroanalytical studies, hence its removal from the system.

4. Toxicity Sensing

4.1 Applications

Since 1976, Hg has been the material of choice for PL monolayer studies because it is the only metal element that is liquid at room temperature [9]. Hg is also highly compatible with the hydrocarbon region of the PL monolayer [34]. When supported by an Hg drop, the PL monolayer is defect free and self-healing, which has allowed extensive studies of phase behaviour [13,16]. This phase behaviour provides the basis for bio-sensing investigations.

Nelson [35] undertook the first study looking at the bio-sensing potential of the adsorbed PL monolayer. The study measured the penetration of the monolayer by polynuclear aromatic hydrocarbons (PAHs), which were chosen because of their toxic effects on marine organisms. Penetration by PAHs did not displace the monolayer but did cause a potential shift in the cathodic capacitance peaks [35]. The most hydrophobic/lipophilic PAHs caused the biggest disruption of the monolayer and registered the greatest potential shift, with a detection limit of 0.4µg/l [35,36].

The same electrode system has been used to further the understanding of voltage dependant ion carriers/ channels in biological membranes [37-39]. Another study by Nelson et al [37] found that the antibiotic ionophore A23187 renders the PL monolayer permeable to Cd^{2+} and Cu^{2+}. The ionophore was embedded into the PL monolayer and formed a complex with the metal ions. At a critical potential, the monolayer + ionophore-metal ion complex undergoes a conformational change that facilitates the translocation of the metal ion from the bulk solution to the electrode surface, where it is reduced. Other protons and cations in the solution can also complex the ionophore, preventing the transport of Cd^{2+} and Cu^{2+}. Similarly, anions that bind strongly to Cd^{2+} and Cu^{2+} in solution, also limit metal ion transport [37].

A study of gramicidin ion channels found that the permeability of thallium (Tl^{+}) ions in PL-gramicidin monolayers adsorbed on Hg were dependant on a number of factors; the specific lipid used, electrolyte pH/charge and the size ratio of the electrolyte cation [38,39]. The earlier study found that negatively charged PS-gramicidin layers were around nine times more permeable to Tl^{+} ions than zwitterionic DOPC-gramicidin

layers [34]. Therefore, DOPC was used in the later studies as it provided a more tightly packed/stable support for proteins [39].

There are two main reasons why biomembrane models are of interest. First, it is well known that many biologically active compounds exert their effect by interacting with ion channels/carriers within the cell membrane [40-43]. Second, there is great interest in designing a sensor that selectively responds to toxic compounds. It has already been shown that selective proteins incorporated into PL monolayers adsorbed on mercury can be used as the sensing element for toxicity detection [35-39]. This system has a wide range of potential applications including, *on-line* toxicity monitoring; military use and for detecting organic species in aircraft linked to deep vein thrombosis (DVT) [44-46].

Despite the exciting potential of PL monolayers on Hg, there are a number of shortcomings that limit the bio-sensing applicability of the system [34]: -

1. It relies on a single analytical method (electrochemistry)
2. The PL monolayer is fragile
3. Hg is highly toxic

As discussed in Chapter-1, Hg has a high affinity for thiol groups, these are found within cysteine amino acid residues and as a result, Hg inhibits/modifies the biological function of many proteins [47,48]. Hg toxicity can also lead to the overproduction of reactive oxygen species (ROS) [49,50]. Hg induced oxidative stress can cause serious damage to cells and has been linked to hypertension, cardiovascular disease and stroke [51]. The neurotoxic effects have also been well documented [52-54].

The eventual aim of this project is to produce an industrial device for *on-line* toxicity sensing. For this reason, it would be preferable to replace Hg with non-toxic alloys of Ga, Ga-In or Ga-In-Sn (galinstan). Not only would this help lower production/regulatory costs, but would also make the device more environmentally friendly and therefore easier to market. Galinstan has already been used as a replacement for Hg in thermometers and has not only solved the toxicity issues but has also been shown to be more accurate than digital devices [53]. Ideally, Ga alloys would not only negate toxicity concerns, but may actually demonstrate enhanced electrochemical characteristics.

4.2 Physical/Chemical Properties of Gallium Alloys

The primary criterion for an Hg replacement for use in electroanalytical studies is a metal that is liquid at room temperature, presenting an atomically flat/ homogenous surface for PL deposition. The eutectic alloys of Ga-In and galinstan have melting points of 15.7°C and -19°C respectively [55,56]. Eutectic refers to the fact that the melting point of the alloy is lower than the melting points of the constituent elements. Ga alloys are also considered non-toxic and have low vapour pressures compared with Hg, reducing the chance of vapour inhalation.

	Hg	**Ga-In**	**Galinstan**
Composition	Pure	21.5% In, 78.5% Ga	68.5% Ga, 21.5% In, 10% Sn
Melting Point	-38.8°C	15.7°C	-19°C
Vapour Pressure	0.1713Pa at 20°C	NA (low [56])	$<10^{-6}$ Pa at 500°C
Density	13.534g cm^{-3}	6.35 g cm^{-3}	6.44g cm^{-3}
Electrical Conductivity	2.30 x 10^{4} S cm^{-1}	3.4 x 10^{4} S cm^{-1}	3.46 x10^{4} S cm^{-1}
Solubility	Insoluble	Insoluble	Insoluble

Table 1. *Properties of liquid metals [57-59]*

4.3 Previous EDL Studies Using Gallium Alloys

Butler and Meehan [60] performed the first EDL study using Ga alloys. The electrochemical characterisation of the double-layer was found to be more complicated due to the occurrence of faradaic processes. They found that the dissolution of Ga from the alloy and the low hydrogen overpotential compared with Hg, were problematic when trying to isolate non-faradaic processes.

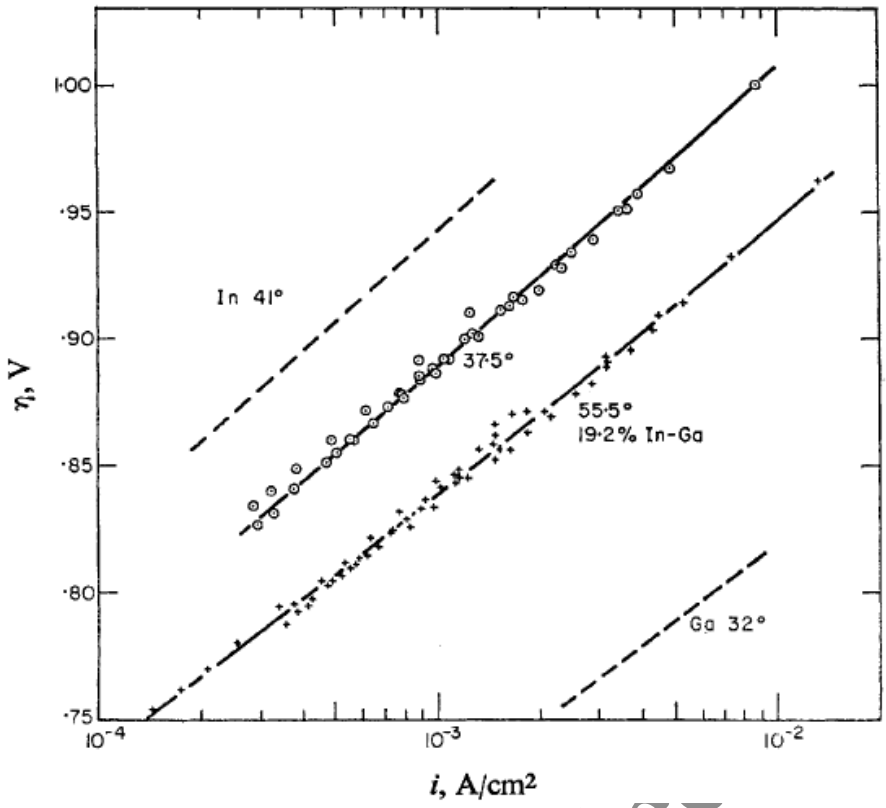

Figure 17. *Overpotentials for Ga (32℃), 19.2% In-Ga (55.5℃/37.5℃) and In (41℃) [61]*

The hydrogen overpotential increases from pure Ga to pure In and with decreasing temperature (Fig 17). The overall effect is that the overpotential of Ga increases by 150mV when 19.2% In is added. A 280mV increase is recorded when 1.64% Hg is added to Ga; the electrolyte used was 0.1M $HClO_4$, versus the NHE. For Ga-In at 37.5^{o}C hydrogen reduction begins at just below -0.8V (Fig 17). Overpotential is the additional potential beyond the thermodynamic requirement ($E^{\ominus}$), needed for a redox reaction to occur at a certain rate. Essentially, overpotential represents the thermodynamic barrier that must be overcome before reduction/oxidation occurs. In this project, the goal is to prevent hydrogen reduction therefore a large barrier to this process (high overpotential) is preferable.

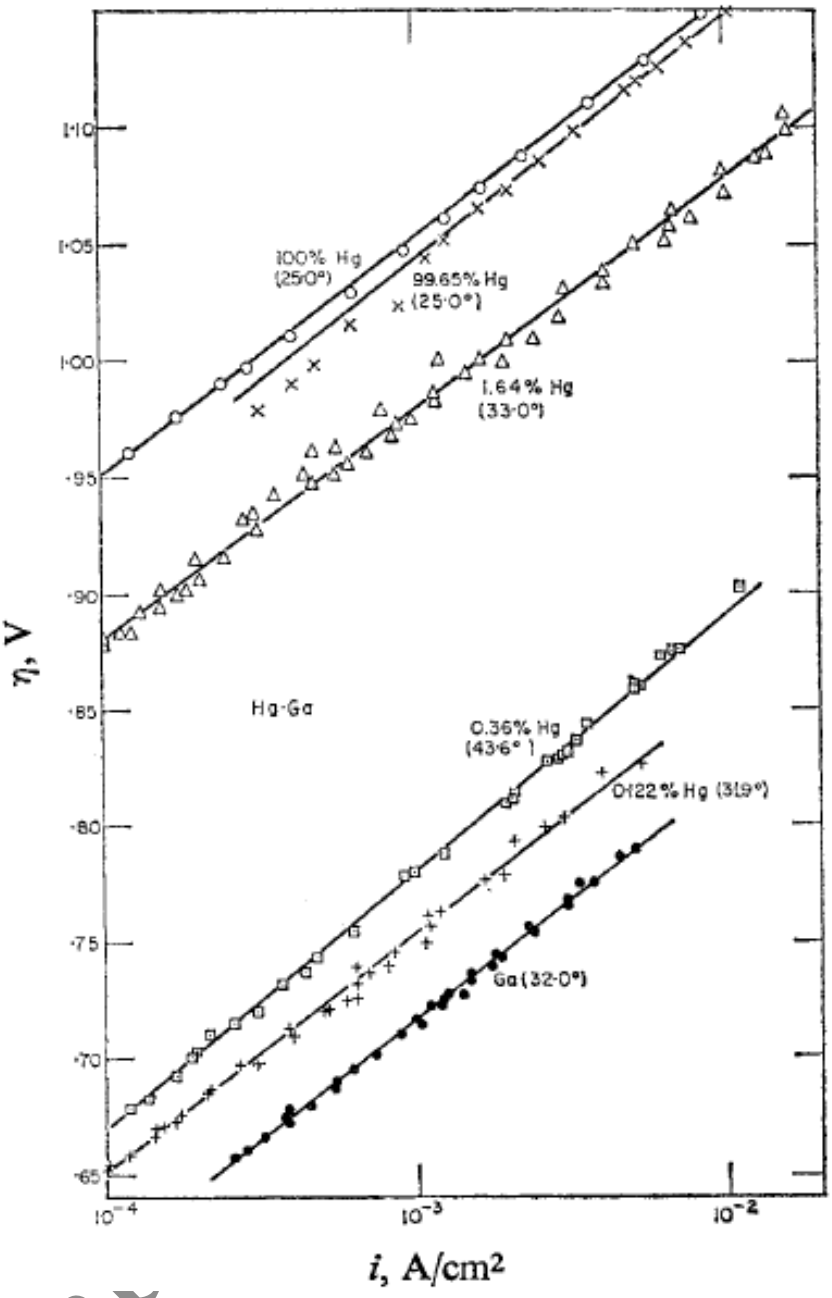

Figure 18. *Comparison of hydrogen overpotentials for gallium alloys and mercury at different temperatures [61].*

The difference in hydrogen overpotential between Ga and Hg (Fig 18) is particularly problematic when trying to deposit PLs because hydrogen bubbles destroy the delicate monolayer. Also, being an irreversible faradaic process, hydrogen reduction interferes with the current associated with double-layer charging making equation 26, void.

Three independent processes were responsible for the current versus time curves measured by Butler and Meehan: double layer charging, hydrogen evolution and dissolution of Ga from the amalgam [60]. The latter were deemed to have little effect on the double-layer charging current. The PZC of 19.2% In-Ga in 0.1M $HClO_4$ versus a reversible H_2 was -0.600V compared with -0.160V for Hg under the same conditions (shifted 440mV more negatively) [61,62]. The previous studies also noted that Hg-Ga alloys had a tendency to separate into two phases and single phase alloys were only obtainable when there was less than 2%wt Hg to Ga or 96.5%wt Hg to Ga [61]. The phase separations as well as the wetting characteristics of oxidised Ga make it difficult to perform traditional dropping/hanging techniques.

Despite problems with oxidation, Surmann and Zeyat [63] successfully used a hanging galinstan drop electrode (HGDE) to detect Cd^{2+} and Pb^{2+} using differential pulse anodic stripping voltammetry (ASV). They found that the limit of detection was between 10^{-4}-10^{-6}M but with changes to the setup, they achieved a good signal at concentrations as low as 10^{-8}M. The ASV peaks for both metals were shifted by 200mV cathodically. A similar investigation by Sivan et al [64] also found that the peaks were shifted by 200mV for bare galinstan. They also measured the I-V characteristics for liquid marbles coated with tungsten trioxide (WO_3), finding that the coating layer created a better response (sharper peaks). The oxide layer was electrochemically removed in both experiments. Without the oxide layer, Liu et al [65] found contact angles on various substrates to be greater than 90^o (non-wetting).

Surmann and Zeyat speculate whether the detection limits of galinstan could be improved by using a film electrode. The problem with liquid metals is that they are corrosive, forming amalgams with a number of metals [63,64]. To prevent corrosion, a number of groups have used the refractory metals tungsten (W) and iridium (Ir) as a conductive support for liquid metals [66-70]. Microfabrication using refractory metals is difficult due to their high melting points, 2450^oC for Ir and 3410^oC for W respectively [71,72]. Dr Z. Coldrick at the University of Leeds spent a considerable amount of time trying to fabricate an Ir electrode array without success. It was decided that Pt would be suitably corrosion resistant for use in this project.

5. Experimental

5.1 Flow-cell and Electrodes

The microfabricated electrodes used in this project consisted of a Pt array deposited onto a Si_4N_3 wafer, with a 30nm titanium (Ti) adhesion layer in between (Fig 19). The Pt and Ti layers are deposited via plasma enhanced chemical vapour deposition (PECVD), which leaves a residue on the surface. Before being used the electrodes were cleaned using ethanol and then rinsed with 18.2MΩ milli-Q ultrapure water to remove any organic species as well as the microfabrication residue. The working electrodes were then electrochemically cleaned using RCV from -0.4V to -3.0V, scan rate $10Vs^{-1}$, with a platinum bar counter electrode and Ag/AgCl reference. The reference electrode used throughout the project was a (3.5mol dm^{-3} KCl, Ag/AgCl inner filling, 0.1mol dm^{-3} perchloric acid outer filling) separated from the electrolyte by a porous sintered glass frit. The working electrode potential was controlled relative to this reference using a research potentiostat.

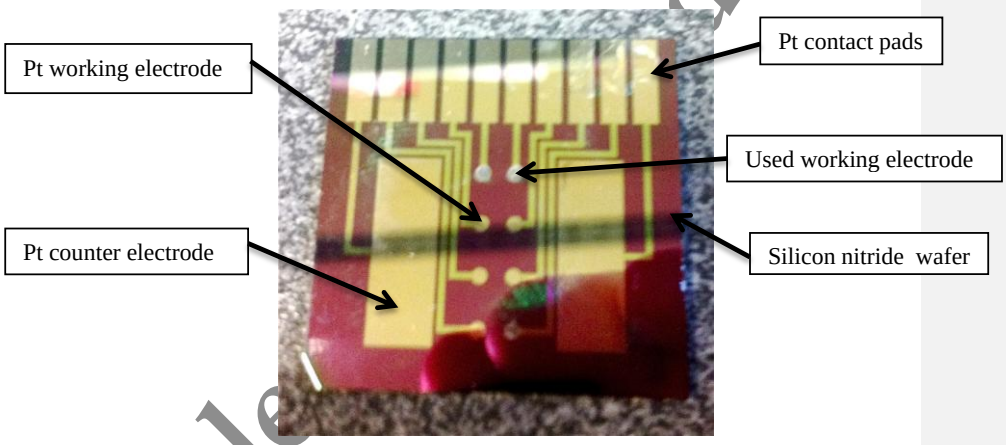

Figure 19. *Pt microelectrode array*

During the first experiments, the deposition of the liquid metal was performed in a glass dish filled with 0.1mol dm^{-3} KCl electrolyte. One problem with this set-up was that the liquid metals tended to run off the angled surface. Another problem was that the electrolyte penetrated the multi-pin connector causing a short circuit. To overcome this, the deposition technique was modified so that the liquid metals could be pipetted onto the array *in-situ*. A polytetrafluoroethylene (PTFE) flow cell housed the electrodes and kept the silicon wafer flat during the electrodeposition of liquid metals

(Fig 20). After the bare electrode had gone through a number RCV cycles using the same potential window and scan rate as electrodeposition, a drop of Hg was pipetted onto the surface. It was found that the Ga alloys adhered better after Hg had been deposited and then removed first.

A)

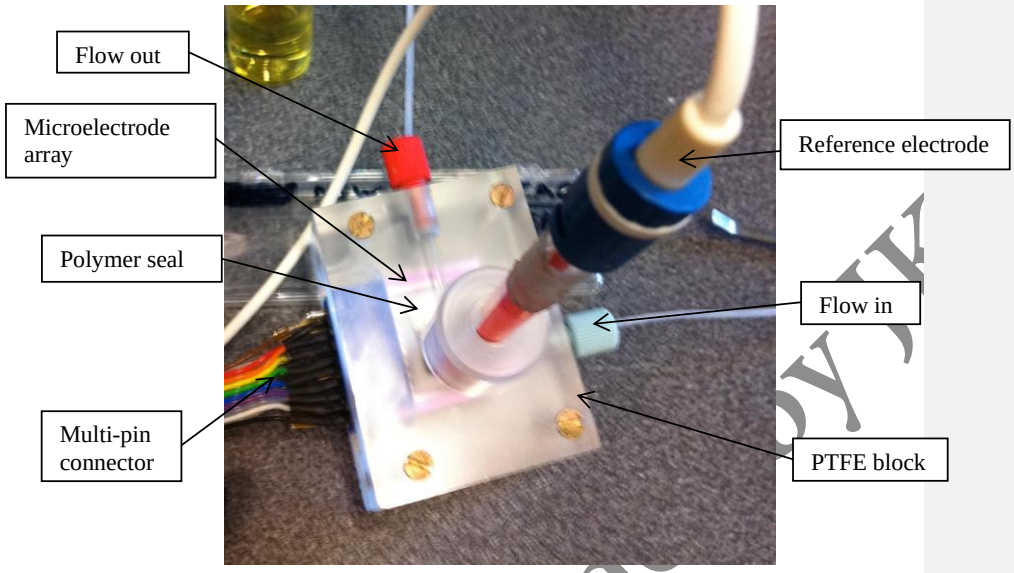

B)

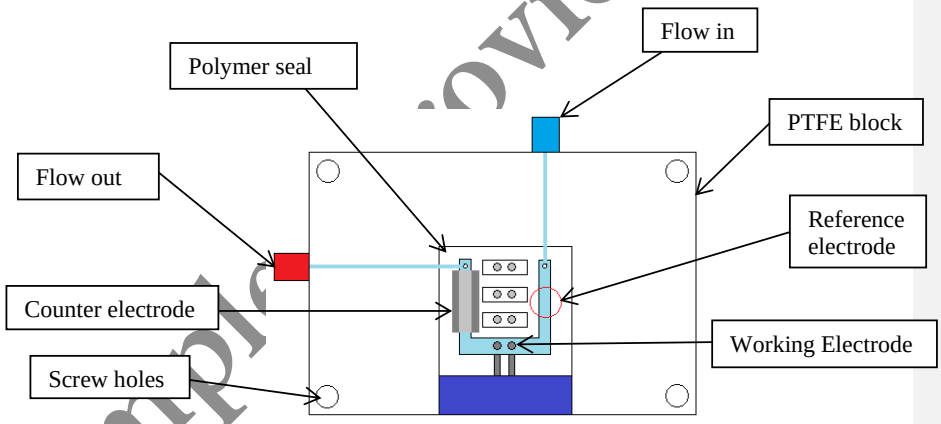

Figure 20. *A) Electrochemical flow-cell, B) Schematic of flow-cell (top-view)*

The counter electrode used during the experiment was a large Pt pad that was also deposited onto the silicon wafer. A polymer patch was specially cut to seal the electrochemical cell, allowing electrolyte to flow across the three-electrodes via two channels in the PTFE block. A rotary pump, connected to a three-way valve controlled

via a switchboard, regulated the electrolyte flow. This was a progression from a previous design that used separate components (Fig 21).

The electrolyte was stored in a 5-litre reservoir containing deaerated 0.1mol dm^{-1} KCl covered in an argon (Ar) blanket layer. Electrolyte was prepared from Analar KCl (Fisher Chemicals ltd) calcined at 600^{o}C. Another smaller reservoir, also with Ar bubbling through, allowed the addition of different solutions/buffers. The switchboard controlled the on/off of flow and determined which reservoir the electrolyte was taken from. One 5ml and one 10ml syringe were connected just upstream of the flow cell, the 5ml syringe contained DOPC from Avanti lipids (1mg/ml in 0.1mol dm^{-3} KCl), whilst the 10ml contained electrolyte and was used to slowly fill the cell immediately after assembly.

The microelectrode array was connected to a PGSTAT12 potentiostat interfaced to a PowerLab 4/25 signal generator (AD instruments ltd) controlled using AutoLab (Electrochemie, Utrecht, Netherlands) and Scope^{TM} software (ACV/RCV respectively).

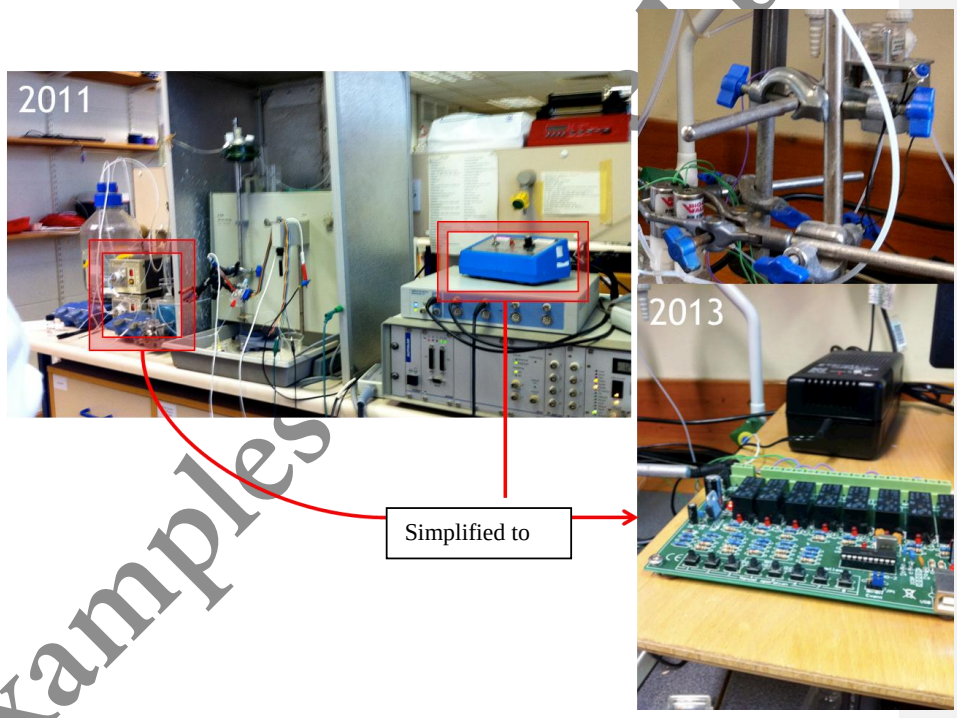

Figure 20. *Development of flow-system*

The following liquid metals were used: -

- 99.99% pure Ga-In (Sigma Aldrich)
- Galinstan (68.5% Ga, 21.5% In, 10% Sn) (Rotometals USA)
- 99.9999% pure electronic grade Mercury (Sigma Aldrich)

Combining Hg with the Ga alloys was difficult due to wetting. During the first attempt, the two components were mixed in an Eppendorf under standard atmospheric conditions. The oxidised Ga metal simply coated the inside walls and the Hg remained in a separate phase at the bottom of the container. Without having an inert gas box, it was decided that the alloys be combined under deaerated 0.1mol dm^{-3} KCl buffer (Fig 21).

Figure 21. *Left: Ga alloy sticking to eppendorf. Right: 11.2%wt galinstan: Hg, combined under deaerated 0.1mol* dm^{-3} *KCl*

The first step involved filling an airtight glass container so that the entire volume was taken up and the liquid was level with the rim. This was then weighed using a digital balance accurate to 0.1mg. The Ga alloys were then pipetted into the container and the change in weight measured. Ga alloys were pipetted first because they stuck to the inside of the pipet tip; Hg was easier to pipet and so compensations could be made more easily. After Hg was added, the container was topped up to full again before being weighed a final time. The amount of KCl displaced by each addition could be calculated from the relative densities of each metal (table 1). This amount was then subtracted from the change in total weight. The density of the 0.1mol dm^{-3} KCl solution was assumed to be 1g cm^{-3}, introducing a small systematic error. Example calculation: -

1) Container full = 29.3301g
2) Ga-In added = 29.3811g
3) Hg added = 29.5266g

$$29.3811\text{g} - 29.3301\text{g} = 0.051\text{g}$$

$$\frac{0.051\text{g}}{6.25\text{gcm}^{-3}} = 0.00816\text{cm}^3 \text{ (KCl volume displaced by GaIn)}$$

$$0.051\text{g} - 0.00816\text{g} = 0.04284\text{g (GaIn)}$$

$$29.5266\text{g} - 29.3811\text{g} = 0.1455\text{g}$$

$$\frac{0.1455\text{g}}{13.534\text{gcm}^{-3}} = 0.01107\text{cm}^3 \text{(KCl volume displaced by Hg)}$$

$$0.1455\text{g} - 0.01107\text{g} = 0.1344\text{g (Hg)}$$

$$\frac{0.04284\text{g (GaIn)}}{0.1344\text{g (Hg)}} \text{ x } 100\% = 32\%\text{wt GaIn: Hg}$$

For pH measurements, a Cyberscan pH110 meter (Eutech Instruments) was first calibrated in the supplied buffer solutions (pH7 and pH10). The pH meter was then suspended in the smaller reservoir. Sodium hydroxide (1mmol dm^{-3}, Fisher Chemicals) was used as an alkali buffer and was injected into the cell using a 10ml syringe suspended directly above the 20ml reservoir.

5.2 ACV

The following AutoLab parameters were used for ACV:-

Equilibration time: 5 seconds
Modulation time: 0.21 seconds
Interval time: 0.61 seconds
Frequency: 75.12 Hz
Phase: -90°
Start potential: -0.8V
End potential: -1.8V
Step potential: 0.005mVs^{-1}
Standby potential: -0.8V

Current versus applied potential scans were taken for the bare working electrodes of Hg, Ga-In, Galinstan and 11.2%wt ~~galinstan~~Galinstan: Hg. DOPC was then added using the 5ml syringe. When fresh DOPC was needed, the flow was switched on during re-insertion of the syringe, this prevented bubbles forming in the cell. RCV was used to deposit the DOPC. For ACV studies on Ga alloys, a potential window from -0.4V to -1.9V was found to be the optimum deposition potential. RCV scans that went to more negative potentials caused hydrogen reduction, seen as cloudiness around the working electrode. Scan rates using multiples of $10Vs^{-1}$ were also optimum, any deviation from this created a noisy signal. Deposition of DOPC took around 30 seconds.

Once deposited, the cell was evacuated using the 10ml syringe containing KCl buffer. For Hg it was acceptable to turn the pump on to remove non-adsorbed DOPC. However, for Ga alloys the monolayer was more fragile and better results were obtained using the syringe. Because two different software programs were used for ACV and RCV (AutoLab/Scope), it was important that only one program was running at once so that damage was not done to the underlying Pt layer. Similarly, it was imperative that the reference electrode was securely implanted into the cell prior to a potential being applied.

5.3 RCV

During the initial RCV studies of Ga alloys, a deposition potential window of -0.4V to -1.9V was used. For the removal of DOPC, the potential window was extended to -2.2V, this created hydrogen bubbles that effectively removed the adsorbed PL. During the cleaning process, the flow was switched on so that desorbed material was instantaneously removed from just above the surface. This method of cleaning was found to be more effective than using more positive potentials. Throughout the experiment, the potential was never allowed to go below -0.4V. This ensured the liquid metal remained attached to the underlying Pt surface and that oxidation processes were prevented. Because Hg has a higher hydrogen overpotential than Ga alloys (Fig 17), the deposition of a DOPC monolayer could occur at potentials as low as -3.0V. For RCV studies using a Ga-In electrode, the optimum potential window for DOPC monolayer deposition was found to be -1.1V to -1.8V.

6. Results and Discussion

6.1 Results

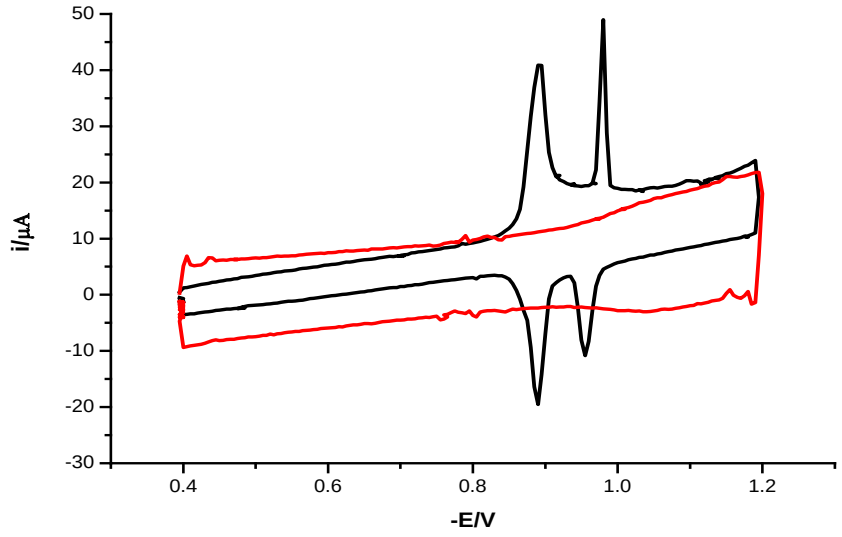

Figure 22. *Overlaid RCV scans recorded at 40Vs^{-1} for a Pt/Hg electrode, red line is the bare electrode, black line is with monolayer (1mg/ml DOPC), (0.1mol dm^{-3} KCl pH 7.4)*

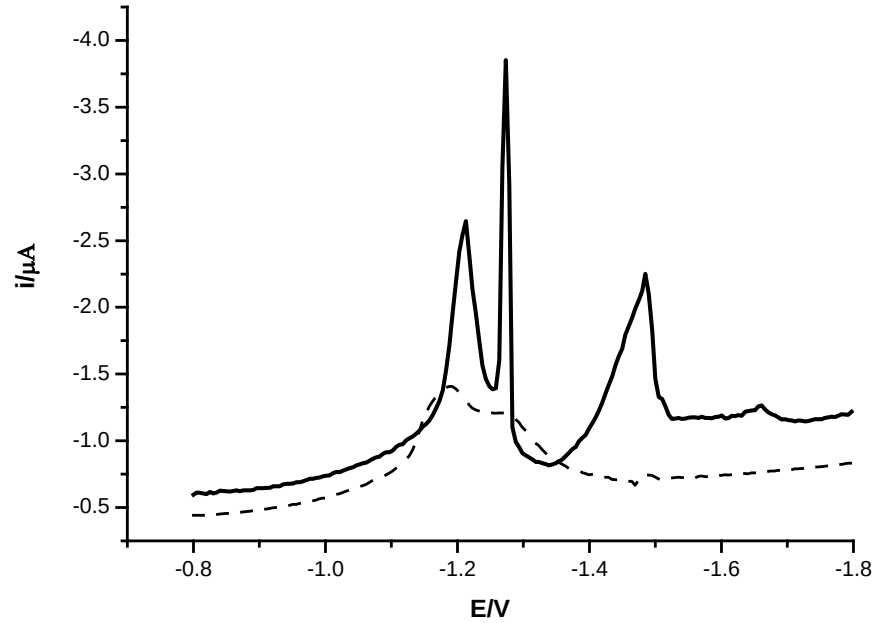

Figure 23. *ACV scan for a Pt/Ga-In electrode, black line is with monolayer (1mg/ml DOPC), dash line is the bare electrode, (0.1mol dm^{-3} KCl pH 7.4)*

Comment [AN1]: Please zero the current axis.

What is the pH?

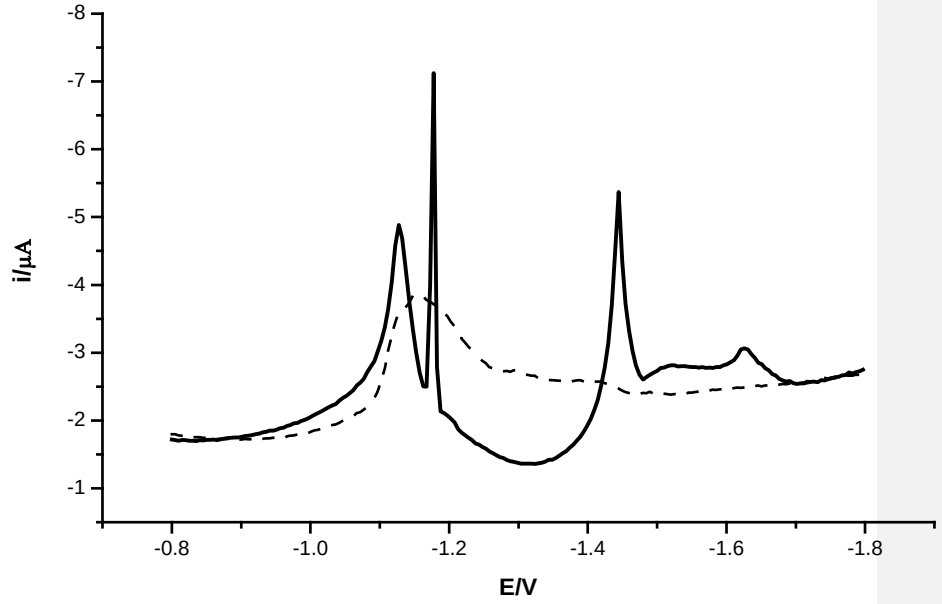

Figure 24. *ACV scan for a Pt/Galinstan electrode, black line is with monolayer (1mg/ml DOPC), dashed line is the bare electrode, (0.1mol dm^{-3} KCl pH 7.4)*

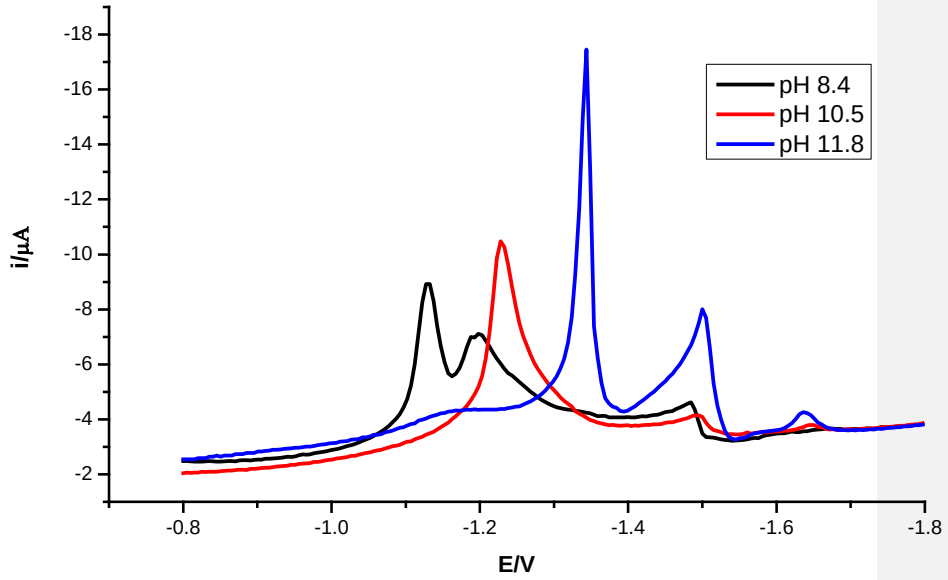

Figure 25. *Overlaid ACV scans for a Pt/Ga-In electrode showing the effect of varying pH on the adsorbed monolayer (1mg/ml DOPC), blue line pH 11.8, red line pH 10.5, black line pH 8.4, (0.1mol dm^{-3} KCl electrolyte, 0.1mol dm^{-3} NaOH alkali buffer)*

Comment [AN2]: Overlay pH 7.4 for comparison.

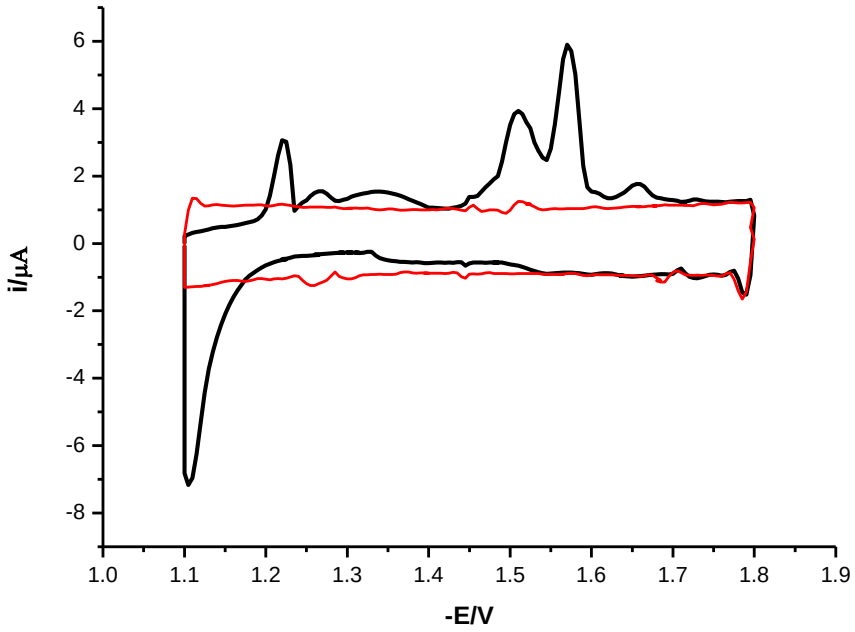

Figure 26. *Overlaid RCV scans recorded at 10Vs^{-1} used for monolayer deposition on Pt/Ga-In electrode, red line is the bare electrode, black line is with monolayer (1mg/ml DOPC), (0.1mol dm^{-3} KCl pH7.4)*

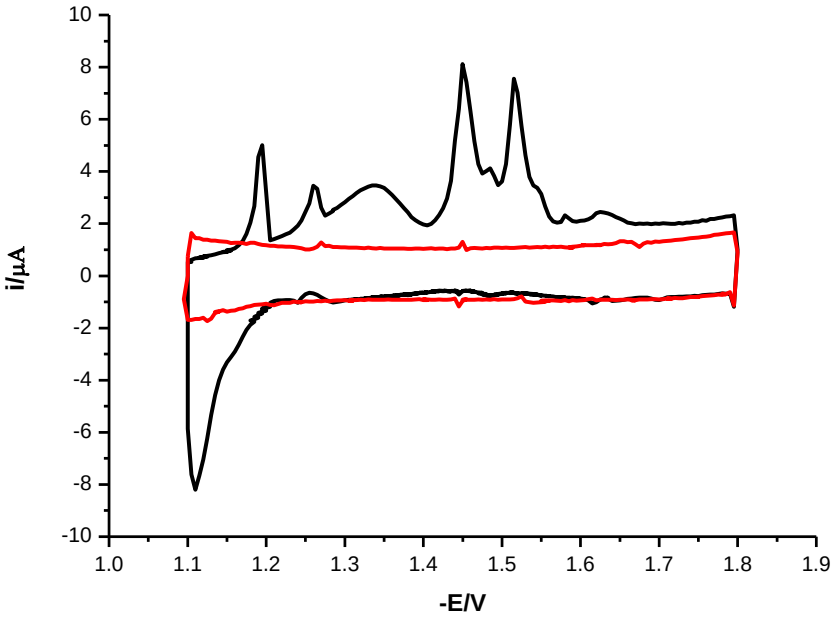

Figure 27. *Overlaid RCV scans recorded at 10Vs^{-1} used for monolayer deposition on Pt/Ga-In electrode, red line is the bare electrode, black line is with monolayer (1mg/ml DOPC), (1.0mol dm^{-3} KCl pH 7.4)*

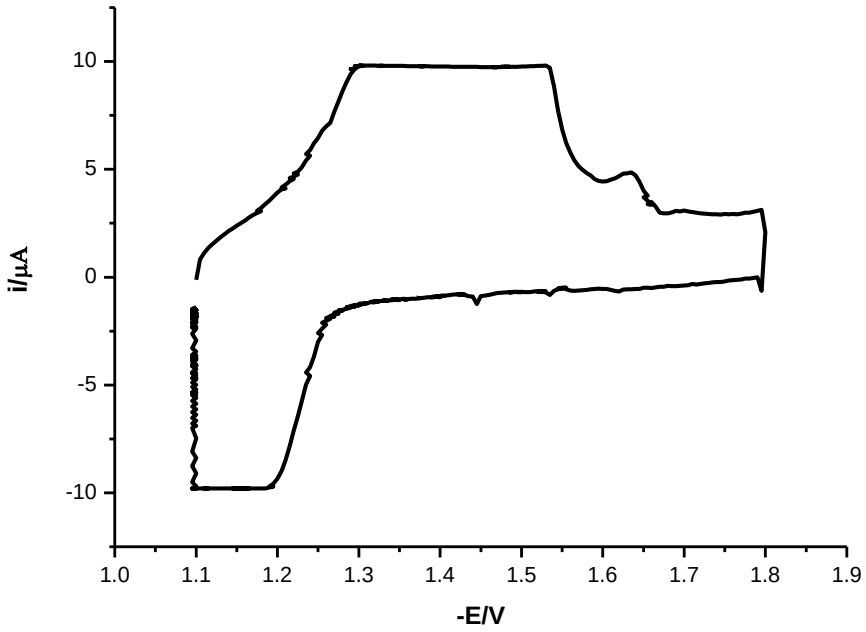

Figure 28. *RCV scan recorded at 10Vs^{-1} for a Pt/Ga-In electrode, flow switched on post monolayer adsorption (1mg/ml DOPC), (0.1mol dm^{-3} KCl pH 7.4)*

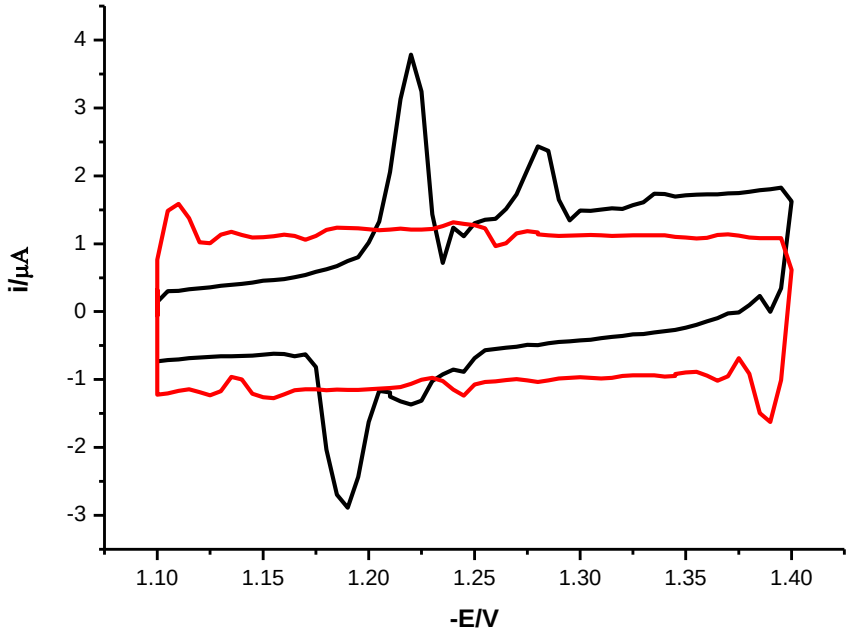

Figure 29. *Overlaid RCV scans recorded at 10Vs^{-1} for a Pt/Ga-In electrode, red line is the bare electrode, black line is with monolayer (1mg/ml DOPC), (0.1mol dm^{-3} KCl pH 7.4)*

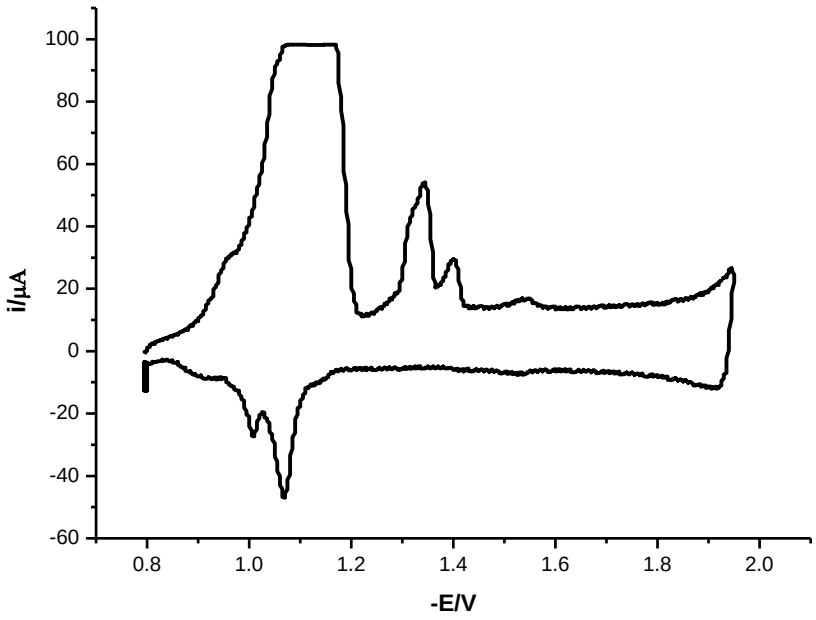

Figure 30. *RCV scan recorded at 10Vs^{-1} for a Pt/11.2%wt galinstan:Hg electrode with monolayer adsorption (1mg/ml DOPC), (0.1mol dm^{-3} KCl pH 7.4)*

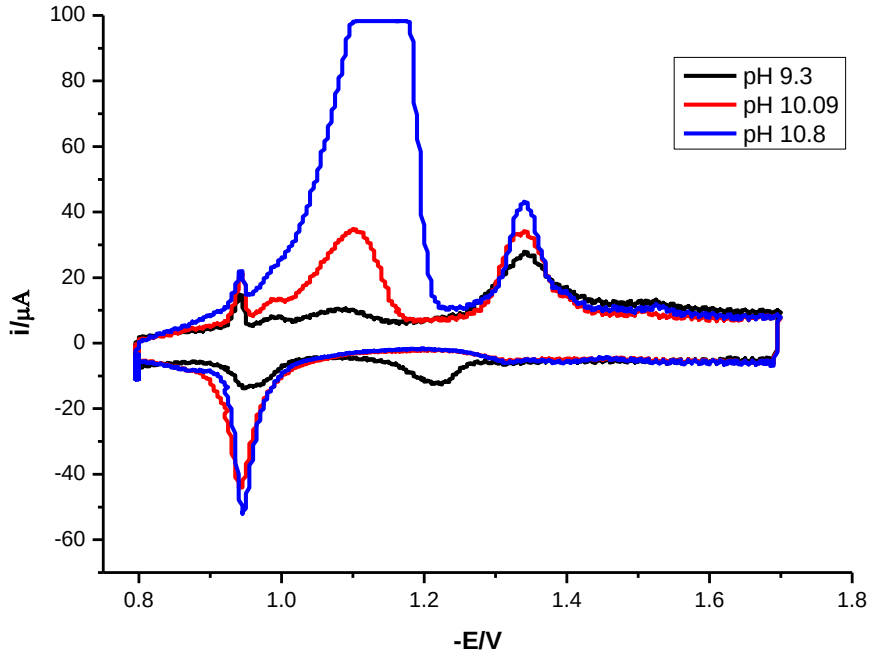

Figure 31. *Overlaid RCV scans recorded at 10Vs^{-1} for a Pt/11.2%wt galinstan:Hg, showing the effect of varying pH on the adsorbed monolayer (1mg/ml DOPC), blue line pH 10.8, red line pH 10.5, black line pH 9.3, (0.1mol dm^{-3} KCl electrolyte, 0.1mol dm^{-3} NaOH alkali buffer)*

6.2 Discussion

The first result (Fig 22) shows an RCV scan using an Hg electrode. This was chosen as a control to see whether the flow cell and electrode setup was functioning correctly. Characteristic phase transitions occured at ~ -0.89V and -0.98V in the cathodic scan, which was in agreement with the literature values [34]. Once the experimental setup was working correctly, the Hg drop was replaced with Ga-In.

The first electroanalytical study of Ga-In was performed using ACV (Fig 23). This technique was chosen because of its improved sensitivity over RCV. The deposition of the monolayer occurred within a -0.4V to -1.9V RCV window. Visible hydrogen reduction was not observed using this potential window. The results show three phase transitions occurring at ~ -1.21V, -1.28V and -1.48V. The three peaks are cathodically shifted by around 300mV compared to Hg. The ACV peaks were reproducible for Ga-In however the sharpest peaks were obtained within the first three scans. After each scan, the monolayer was electrochemically/ physically removed and a new one deposited using RCV. It was found that disconnecting the electrode for a few minutes with the flow on and then reconnecting, gave better reproducibility. This suggests that some residual DOPC or other interfering species remained adsorbed whilst the potential was being held at -0.4V. Any adsorbed species would affect the stored charge density in the Stern layer, reducing the change in capacitance, thus producing broader/less defined peaks.

The same experiment was then repeated using a galinstan electrode. Figure-24 again shows sharp phase transition peaks, this time at ~ -1.13V, -1.18V and -1.44V. For galinstan, the three peaks are cathodically shifted by 200mV compared with Hg, which is in agreement with Surmann and Zeyat [63] who observed a similar shift when detecting Cd^{2+} and Pb^{2+} using ASV. Despite the sharp peaks, the monolayer was much less stable on galinstan and only one sharp result was obtained. RCV scans using Ga-In and galinstan produced a large current peak at just below -0.8V. The peak was greater for galinstan and was assumed to be hydrogen reduction. In an attempt to suppress this reduction, NaOH was used as an alkali buffer. It was expected that hydrogen reduction would decrease as the concentration of H^+ ions fell, however high pH had the opposite effect.

Figure-31 shows that the supposed hydrogen peak increases at high pH. This implies that it is not hydrogen reduction but some other faradaic or non-faradaic process,

possibly some contamination. The ACV plots in figure-25 also show that the three phase transitions are shifted to more negative potentials as pH increases. The ACV plot for Ga-In (Fig 25) shows that the first phase transitions relating to pore-formation are lost at high pH [13]. This effect may be a result of adding Na^+ ions to the electrolyte. The increased concentration of cations in solution may prevent pore formation. Instead, the monolayer is rapidly penetrated by the counter-ions and is therefore recorded as a single surface event (Fig 3).

A repeat experiment using a different buffer such borate would be needed to confirm this. At more negative potentials (~ -2.9V), the high pH electrolyte created a black coating on the Ga-In electrode that resembled an oxide layer. This could be removed by switching to a more positive voltage, although a black residue remained. This may in fact be Na^+ reduction, which occurs at (-2.71V vs SHE). Na^+ reduction at a DME has been shown to be accompanied by an irreversible process whereby a chemical reaction occurs between the Hg/Na amalgam and water [73]

Despite the fact that no RCV peaks were obtained with pure galinstan, an 11.2%wt mix with Hg did produce peaks. Figure-30 shows two cathodic peaks at ~ -1.34V and -1.40V these also appear in the anodic scan at ~ -1.01V and -1.07V. This is comparable to where the third peak is seen in the ACV plot of pure galinstan (Fig 24). The literature suggests that this third ACV peak is related to desorption, where the monolayer leaves the electrode surface. However, a recent AFS study by Dr A. Vakourov shows that the PL is still present on the surface after the desorption peak. This suggests that another process is occurring at this potential, possibly the compression of the bilayer. Another suggestion was the re-orientation of the monolayer, with the hydrocarbon chains facing into the solution. Under standard conditions this would be extremely unfavourable due to the decrease in entropy associated with the constraining water molecules around the apolar segments (clathrate cages). This would yield very positive values for Gibbs free energy. Further analysis would be required in order to determine the compression hypothesis.

Following on from the work of Butler and Meehan [60-62], a number of different ratios of Ga alloys to Hg were tested. No RCV or ACV peaks were obtained for mixes of more than 11.2%wt, for both Ga-In and galinstan. There was an anomalous result using a 30%wt Ga-In: Hg combination. Very sharp and stable phase transitions were recorded that did not show any shift in potential and were exactly the same as those of

mercury (Fig 22). It is likely that the two metals had simply separated into two phases and the electrode was predominantly mercury.

In order to avoid suspected hydrogen reduction, the RCV potential window used to deposit the monolayer on Ga-In was shifted (-1.1V to -1.8V). The focus of the project moved towards Ga-In because of the greater monolayer stability/reproducibility. Figure-26 shows overlaid RCV plots for the bare Ga-In electrode and adsorbed monolayer. In order to obtain a stable RCV scan, the pump was switched off for the removal of excess/non-adsorbed DOPC. Instead, the cell was evacuated using the 10ml syringe filled with electrolyte. The detrimental effect of turning the pump on can be seen in figure-28. Again a large, disruptive peak occurs as new electrolyte enters the cell at increased flow rates. Under quiescent conditions, the RCV scan remained stable. This suggests that the exponential decay of charge density (equation 20) within the diffuse layer extends further into the solution than with Hg. The flow didn't wash away the monolayer because when it was turned off the peaks returned, which means the monolayer was still adsorbed. Sharper peaks were observed with increased concentrations of electrolyte (Fig 27). However, the hump at -1.3V became more pronounced and so 0.1mol dm^{-3} electrolyte was used for the remainder of the experiment.

The stable phase transition peaks in figures 26 and 27, compare favourably with those obtained with Hg [13, 34]. Figure-32 translates the theoretical model of PL phase transitions on Hg (Fig 3) with those obtained for Ga-In.

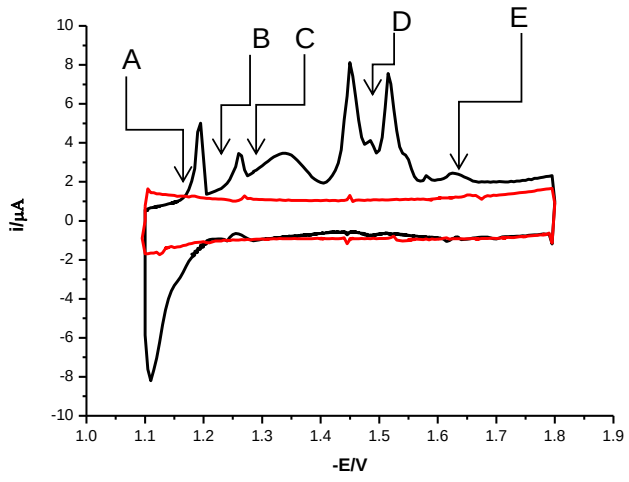

Figure 32. *Pt/Ga-In electrode, A) Intact monolayer, B) Pore formation, C) Porous monolayer, D) Bilayer and micelles, E) Vesicles/desorption*

Once the monolayer deposition conditions had been optimised, the potential was shifted to a smaller range (-1.1V to -1.4V). Using this potential window it was possible to obtain stable phase transitions similar to those of Hg, albeit negatively shifted. As already stated, these phase transitions relate to changes in the capacitance of the double layer however, all the RCV scans in this report plot current versus voltage. To calculate capacitance, one would have to calculate the area of the electrode. This can be done either electrochemically or via microscopy techniques such as Scanning Electron Microscopy (SEM). Assuming an absence of faradaic process the phase transitions can be attributed to changes in capacitance, since capacitance is directly proportional to current (equation 26).

An attempt was made to measure the PZC of the Ga-In electrode using ACV and low concentrations of electrolyte. Using the microelectrode 'chip' array, it was not possible to get the characteristic dip in capacitance as described in section 2.1. It was supposed that the exposed Pt support layer prevented PZC measurements in what should otherwise be a straightforward procedure. The reasoning behind this is that Pt is a polycrystalline solid, which has inherent problems when studying stored charge density (section 2.2).

As mentioned in section 4.3, liquid metals are corrosive to Pt. The Pt/Ga alloy electrodes lasted for around two weeks, before the underlying Pt was corroded away. In figure-19, the working electrode has been corroded away by Ga-In. Once this occurred the alloy no longer adhered to the surface and the electrode no longer functioned.

6.3 Conclusion

This project demonstrates that the eutectic Ga-In alloy can be used as a PL monolayer support. The phase transition peaks previously seen on Hg were also seen on Ga-In, opening up an exciting new area of electrochemical research whereby toxic Hg is replaced by a safer alternative. This is the first time that Ga alloys have been used on a microelectrode array connected in a flow-through system, which negates the problems associated with traditional drop techniques and Ga oxidation.

The flow-through system has developed a lot over the last few years and has exciting potential for toxicity monitoring. With water supplies coming under greater pressure

from modern industrial processes, there is a great need for new bio-sensing devices. The widespread use of nanomaterials in everyday consumer goods has yet unknown environmental consequences. How these nanomaterials interact with cell membranes is especially important, as this is a key barrier that potentially toxic compounds must overcome. A PL monolayer adsorbed onto the surface of the electrode mimics the outer leaflet of a lipid bilayer, providing a simple but effective membrane model. The incorporation of cell membrane proteins including ion-carriers/ channels has already been studied but the potential of this has not yet been fully explored.

Despite the relative simplicity of using well-established electroanalytical modalities, the complexities of the monolayer phase transitions are still not fully understood. Recent evidence from modern microscopy techniques has highlighted some discrepancies in the theoretical predictions stemming from mean-field theory and Monte Carlo simulations. This is an exciting new discovery that re-opens the debate as to what the third capacitance peak, observable on both Hg and now Ga alloys, actually represents.

6.4 Future Work

Now that phase transitions have been achieved on Ga-In using both RCV and ACV, there are number of future projects that can stem from this. The first concern would be to find out what the current peak attributed to hydrogen reduction actually represents and if it proves to be hydrogen, how can it be suppressed without affecting the phase transitions. The idea of using high pH would be the logical solution and a number of different buffers would have to be tried, starting with borate.

The current/capacitance peaks from RCV are not as high as those of Hg, which means the self-assembly mechanism is not as strong. To increase the hydrophobic effect, different PLs could be tried. One possibility is the use of superhydrophobic fluorocarbons as a replacement for the hydrocarbon based DOPC. However, whilst replacing toxic Hg from the system a new toxin would be introduced. A recent study of the electrodeposition of polymer films found that certain hydrocarbons could achieve similar levels of hydrophobicity as fluorocarbons (less expensive and environmentally favourable) [74].

Finally, if the microelectrode setup used in this project is to fully realise its industrial potential, then the Pt array will have to be replaced by a more corrosion resistant

metal. Therefore, it would be of great interest to see whether the same microelectrode array could be fabricated from either Ir or W.

(10, 533 words)

References

[1] D. Mandler, S. Kraus-Ophir, *Self-assembled monolayers for electrochemical sensing,* (2011), J. Solid. State. Electrochem. 15: 1535-1558

[2] J. Sagiv, *Organised monolayers by adsorption. 1. Formation and structure of oleophobic mixed monolayers on solid surfaces,* (1980), J. Am. Chem. Soc. 102(1): 92-98

[3] P. Skladel, *Advances in electrochemical immunosensors,* (1997), Electroanalyis, 9(10): 737-745

[4] R. K. Kobos, *Enzyme-based electrochemical biosensors,* (1987), Trends. anal. chem, 6(1):7-9

[5] N. Muskal, I. Turyan, D. Mandler, *Self-assembled monolayers on mercury surfaces,* (1996), J. Electroanal. Chem. 409(1-2):131-136

[6] K. Slowinski, R. V. Chamberlain, G. J. Miller, M. Majda, *Through-band and chain-to-chain coupling. Two pathways in electron tunnelling through liquid alkanethiol monolayers on mercury electrodes,* (1997), J. Am. Chem. Soc. 119:11910-11919

[7] O. Magnussen, B. Ocko, M. Deutch, M. Regan, P. Persham, D. Abernathy, G. Grübel, JF. Legrand, *Self-assembly of organic films on a liquid metal,* (1996), Nature, 250-252

[8] R. Weast, M. Arstle, W. Beyer, *CRC handbook of chemistry and physics,* (1986), Boca Raton, 174-184

[9] I. Miller, J. Rishpon, A. Tenenbaum, *Electrochemical determination of structure and interactions in spread lipid monolayers,* (1976), Bioelectrochemistry and bioenergetics, Elsevier, 3(3-4):528-542

[10] A. Nelson, A. Benton, *Phospholipid monolayers at the mercury/water interface,* (1986), J. Electroanal. Chem. 202:253-270

[11] D. Bizzotto, A. Nelson, *Continuing electrochemical studies of phospholipid monolayers of dioleoyl phosphatidylcholine at the mercury-electrolyte interface,* (1998), Langmuir, 14:6269-6273

[12] A. Nelson, D. Bizzotto, *Chronoamperometric study of T1(I) reduction at gramacidin-modified phospholipid-coated mercury electrodes,* (1999), Langmuir, 15: 7031-7039

[13] A. Brukhno, A. Akinshina, Z. Coldrick, A. Nelson, S. Auer, *Phase phenomena in supported lipid films under varying electric potential*, (2011), Soft. Mat. 7:1006-1017

[14] P. Beer, P. Gale, D.Smith, *Supramolecular interactions*, (2003), Oxford Uni Press

[15] J. Israelachvili, *Intermolecular and surface forces*, (2011), Elsevier, 3rd edition

[16] F. Leermakers, A. Nelson, *Substrate-induced structural changes in electrode-adsorbed lipid layers*, (1990), J. Electroanal. Chem, 278:53-72

[17] J. Fried, *Polymer science and technology*, (2003), J. Chem. Edu, 2nd edition

[18] U. W. Gedde, *Polymer Physics*, (1999), Kluwer, 3rd edition

[19] L. Robeson, *Polymer blends: a comprehensive review*, (2007), Hamer

[20] P. Flory, *Thermodynamics of high polymer solutions*, (1941), J. Chem. Phys, 9(8):660

[21] M. Huggins, *Solutions of long chain compounds*, (1941), J. Chem. Phys, 9(5):440

[22] S. Martens, H. McMahon, *Mechanisms of membrane fusion: disparate players and common principles*, (2008), Nat. Rev. Mol. Cell. Biol. 9:543-556

[23] T. Mills, J. Huang, G. Feigenson, J. Nagle, *Effects of cholesterol and unsaturated DOPC lipids on chain packing of saturated gel-phase DPPC bilayers*, (2009), Gen. Physiol, Biophys, 28(2): 126-139

[24] H. Goldfine, *Bacterial membrane and lipid packing theory*, (1984), J. Lipid. Research. 25:1501-1507

[25] http://lipidlibrary.aocs.org/plantbio/phosphoinositide/Figure2.png accessed 25/03/2013

[26] A. Bard, L. Faulkner, *Electrochemical methods*, (2001), Wiley, 2nd edition, chapters 2,3 and 13

[27] J. Wang, *Analytical electrochemistry*, (2000), Wiley, 2nd edition, chapter 2

[28] D.C. Grahame, *The electrical double layer the theory of electrocapillary*, (1947), Chem. Rev. 41, 441

[29] E. Gileadi, *Interfacial electrochemistry: an experimental approach*, (1975), Addison-Wesley. Pub. Co

[30] P. Rieger, *Electrochemistry*, (1994), Chapman & Hall, 2nd edition

[31] H. Friedmann, O. Amiri, A. Aït-Mokthar, *Physical modelling of the electrical double layer effect on multispecies ion transport in cement-based materials*, (2008), Cement and concrete research, Elsevier, 38(12):1394-1400

[32] R. Compton, C. Banks, *Understanding Voltammetry*, (2011), Imperial College Press, 2nd edition

[33] D. K. Gosser Jr, *Cyclic voltammetry simulation and analysis of reaction mechanisms,* (1993), Wiley-VCH, New York

[34] Z. Coldrick, P. Steenson, P. Millner, M. Davies, A. Nelson, *Phospholipid monolayer coated microfabricated electrodes to model the interaction of molecules with biomembranes,* (2009), Electrochimic. Acta. 54:4954-4962

[35] A. Nelson, *Penetration of mercury-adsorbed phospholipid monolayers by polynuclear aromatic hydrocarbons,* (1987), Anal. Chem. Acta, 194:139-149

[36] A. Nelson, N. Auffret, J. Readman, *Initial applications of phospholipid-coated mercury electrodes to the determination of polynuclear aromatic hydrocarbons and other organic micropollutants in aqueous systems,* (1988), Anal. Chim. Acta. 207: 47-57

[37] A. Nelson, *Electrochemical studies of antibiotic 23187 (A23187) mediated permeability to divalent heavy-metals in phospholipid monolayers adsorbed on mercury electrodes,* (1991), J. Chem. Soc. Faraday. Trans. 87(12): 1851-1856

[38] A. Nelson, *Effect of lipid charge and solution composition on the permeability of phospholipid-gramacidin monolayers to Ti,* (1993), J. Chem. Soc. Faraday. Trans. 89: 2799-2805

[39] A. Nelson, *Conducting gramicidin channel activity in phospholipid monolayers,* (2001), Biophys. J. 80(60): 2694-2703

[40] N. Franks, W. Lieb, *Molecular and cellular mechanisms of general anaesthesia,* (1994), Nature, 367: 607-614

[41] N. Franks, W. Lieb, *Selectivity of general anaesthesia: a new dimension,* (1997), Nat. Med. 3:377-378

[42] B. Hendry, J. Elliot, D. Haydon, *Further evidence that membrane thickness influences voltage-gated sodium channels,* (1985), J. Bio. Phys, 47:841-845

[43] N. Franks, W. Lieb, *Backgorund K^+channels an important target for volatile anaesthetics?,* (1999), Nat. Neurosci. 2:395-396

[44] J. Ayres, R. Harrison, G. Nichols, R. Maynard, *Environmental medicine,* (2010), Hodder Arnold, 249-250

[45] P. Upham, *Towards sustainable aviation,* (2003), Earthscan Publications, 49-50

[46] B. Martin, D. Hocking, *Air quality in airplane cabins and similar enclosed spaces,* (2005), Springer

[47] R. Zalups, L. Lash, *Advances in understanding renal transport and toxicity of mercury,* (1994), J. Tox. Environ. Health. 42:1-44

[48] L. Lash, D. Putt, R. Zalups, *Influence of exogenous thiols on inorganic mercury-induced injury in renal proximal and distal/ tubular cells from normal and uninephrectomized rats,* (1999), 291(2):492-502

[49] O. InSug, S. Datar, C. Koch, M. Shapiro, B. Shenker, *Mercuric compounds inhibit human monocyte function by inducing apoptosis: evidence for formation of reactive oxygen species, development of mitochondrial membrane permeability transition and loss of reductive reserve,* (1997), Toxicology, 31(3): 211-224

[50] L. Patrick, *Mercury toxicity and antioxidants: Part I: Role of glutathione and alpha-lipoic acid in the treatment of mercury toxicity,* (2002), Alternative. Med. Rev, 7(6): 456-469

[51] M. Houston, *The role of mercury and cadmium heavy metals in vascular disease, hypertension, coronary heart disease and myocardial infarction,* (2007), Alternative. Therapy. Health. Med. 13(2): 128-133

[52] M. Aschner, J.L. Aschner, *Mercury neurotoxicity: mechanisms of blood-brain barrier transport,* (1990), Neurosci. Biobehv. Rev. 14(2): 169-176

[53] L. W. Chang, *Neurotoxic effects of mercury: A review,* (1977), Environmental Research 14(3): 329-373

[54] S. Ceccatelli, M. Aschner, *Methylmercury and neurotoxicity,* (2012), Current topics in neurotoxicity, Vol 2, Springer

[55] http://www.sigmaaldrich.com/catalog/product/aldrich/495425?lang=en&region=GB accessed 02/05/2013

[56] http://www.rotometals.com/product-p/lowmeltingpoint-2.htm accessed 02/05/2013

[57] R. Chiechi, E. Weiss, M. Dickey, G. Whitesides, *Eutectic gallium-indium (EGaIn): A moldable liquid metal for electrical characterisation of self-assembled monolayers,* (2008), Angew. Chem. Int. Ed. 47: 142-144

[58] T. Liu, P. Sen, CJ. Kim, *Characterisation of non-toxic liquid-metal alloy galinstan for applications in microdevices,* (2012), J. Microelectromechanical systems, 21(2): 443-450

[59] G. Weissler, R. Carlson, *Vacuum physics and technology,* (1979), Academic press, Vol 14

[60] J. Butler, M. Meehan, *Electrical double-layer measurements on liquid gallium, indium-gallium, and mercury-gallium alloys,* (1966), J. Phys. Chem. 70: 3582-3587

[61] J. Butler, M. Meehan, *Hydrogen evolution on gallium, gallium-indium and mercury-gallium electrodes,* (1966), Trans. Faraday Soc. 62: 3524-3534

[62] J. Butler, *The zero charge potential of indium amalgams in perchloric acid,* (1966), J. Phys. Chem. 77: 2313-2338

[63] P. Surmmann, H. Zeyat, *Voltammetric analysis using a self-renewable non-mercury electrode,* (2005), Anal. Bioanal. Chem. 383: 1009-1013

[64] V. Shivan, SY Tang, A. O'Mullane, P. Petersen, N. Eshtiagi, K. Kalantar-zadeh, A. Mitchell, *Liquid metal marbles,* (2013), Adv. Funct. Mater. 23: 144-152

[65] T. Liu, P. Sen, CJ Kim, *Characterisation of non-toxic liquid-metal alloy galinstan for applications in microdevices,* (2012), J. Micromechanical. Systems. 21(2): 443-450

[66] S. Kounaves, J. Buffle, *Deposition and stripping properties of mercury on iridium electrodes,* (1986), J. Electrochem. 133(12): 2495-2498

[67] M. Nolan, S. Kounaves, *Microfabricated array of indium microdisks as substrate for direct determination of* Cu^{2+} *or* Hg^{2+} *using square-wave anodic stripping voltammetry,* (1999), Anal. Chem. 71: 3567-3573

[68] S. Kounaves, W. Deng, *Analytical utility of the iridium-based mercury ultramicroelectrode with square-wave anodic stripping voltammetry,* (1993), Anal. Chem. 65: 375-379

[69] H. Takahashi, J. Suzurikawa, M. Nakao, F. Mase, K. Kaga, *Easy-to-prepare assembly of tungsten microelectrodes,* (2005), Trans. Biomed. Eng. 52(5): 952-956

[70] M. Nolan, S. Kounaves, *Failure analysis of microfabricated iridium electrodes in chloride media,* (1998), Sensor and actuators, 50(2): 117-124

[71] http://www.sigmaaldrich.com/catalog/product/aldrich/209686?lang=en&region=GB accessed 02/05/2013

[72] http://www.sigmaaldrich.com/catalog/product/aldrich/267538?lang=en&region=GB accessed 02/05/2013

[73] R. Reeves, M. Shuyters-Rehbach, J. Shuyters, *Electrode processes at mercury in the far cathodic region,* (1971). J. Electroanalytical Chemistry and Interfacial Electrochemistry, 34(1): 69-79

[74] T. Darmanin, E. Taffin de Givenchy, S. Amigomi, F. Guittard, *Hydrocarbon versus fluorocarbon in the electrodeposition of superhydrophobic polymer films,* (2010), Am. Chem. Soc. 26(22): 17596-17602